A DIGITALLY CONTROLLED FM MEMS GYROSCOPE SYSTEM

A THESIS SUBMITTED TO
THE GRADUATE SCHOOL OF NATURAL AND APPLIED SCIENCES
OF
MIDDLE EAST TECHNICAL UNIVERSITY

BY

FERHAT YEŞİL

IN PARTIAL FULFILLMENT OF THE REQUIREMENTS
FOR
THE DEGREE OF DOCTOR OF PHILOSOPHY
IN
ELECTRICAL AND ELECTRONIC ENGINEERING

JANUARY 2023

Approval of the thesis:

A DIGITALLY CONTROLLED FM MEMS GYROSCOPE SYSTEM

submitted by **FERHAT YEŞİL** in partial fulfillment of the requirements for the degree of **Doctor of Philosophy** i**n Electrical and Electronic Engineering, Middle East Technical University** by,

Prof. Dr. Halil Kalıpçılar
Dean, Graduate School of **Natural and Applied Sciences** _____

Prof. Dr. İlkay Ulusoy
Head of the Department, **EEE, METU** _____

Prof. Dr. Tayfun Akın
Supervisor, **EEE, METU** _____

Examining Committee Members:

Prof. Dr. Haluk Külah
Electrical and Electronics Eng., METU _____

Prof. Dr. Tayfun Akın
Electrical and Electronics Eng., METU _____

Assoc. Prof. Dr. Kıvanç Azgın
Mechanical Engineering, METU _____

Asst. Prof. Dr. Erdinç Tatar
Electrical and Electronics Eng., Bilkent University _____

Asst. Prof. Dr. Serdar Tez
Electrical and Electronics Eng., Pamukkale University _____

Date: 24.01.2023

I hereby declare that all information in this document has been obtained and presented in accordance with academic rules and ethical conduct. I also declare that, as required by these rules and conduct, I have fully cited and referenced all material and results that are not original to this work.

Name Last name : Ferhat Yeşil

Signature :

ABSTRACT

A DIGITALLY CONTROLLED FM MEMS GYROSCOPE SYSTEM

Yeşil, Ferhat
Doctor of Philosophy, Electrical and Electronic Engineering
Supervisor: Prof. Dr. Tayfun Akın

January 2023, 110 pages

This dissertation presents a digitally controlled high performance FM MEMS gyroscope system with improved short and long term stability for tactical and near navigation grade applications. The digital gyroscope system has a number of advantages such as simplified electronic hardware, small size, low power, and increased flexibility with software programming for easy configuration for different operation conditions, real-time advanced calibration, and extensive testability. The system is implemented with a low-power microcontroller as opposed to the FM MEMS gyroscope systems implemented with high-power FPGAs in literature, and it is fit into a compact sensor package comparable in the size of the commercial high-performance MEMS gyroscopes so that it can be offered as a commercialized product.

The system is developed for a MEMS gyroscope that has a mechanical resonant frequency of about 7.5kHz, which requires digital control loop speeds faster than 75kHz for the 8 implemented digital control loops. These challenging digital control loop speeds are achieved using hardware accelerators and register-level programming methods. The most critical digital control loop is the PLL loop that is used for frequency reading of the FM output, and this loop is carefully designed for

obtaining a measurement bandwidth greater than 100Hz which is necessary for the implementation of the Lissajous FM method to achieve an improved bias instability of the gyroscope. The angular random walk (ARW) performance of the gyroscope is improved significantly by using the Lissajous FM method with an asymmetric MEMS gyroscope for the first time in the literature; as this approach allows to obtain an oscillation amplitude ratio of the first and second resonant modes as high as 2500 (as opposed to values lower than 25 in fully symmetric gyroscope structures) which yields to a record high scale factor of 875Hz/(rad/sec), i.e., two orders of magnitude higher than those reported for the FM MEMS gyroscopes in literature.

The performance of the FM MEMS gyroscope system is measured to provide an ARW value of 0.52°/hr/√Hz and bias instability value of 0.2°/hr, demonstrating about 6 times better performance for each value of the best FM MEMS gyroscope system reported in the literature implemented with a high-power and bulky FPGA board.

Keywords: MEMS, FM gyroscope, MEMS Gyroscope, Digital Control

ÖZ

DİJİTAL OLARAK KONTROL EDİLEN FM MEMS DÖNÜÖLÇER SİSTEMİ

Yeşil, Ferhat
Doktora, Elektrik ve Elektronik Mühendisliği
Tez Yöneticisi: Prof. Dr. Tayfun Akın

Ocak 2023, 110 sayfa

Bu tez, taktiksel ve seyrüsefer seviyeli uygulamalar için geliştirilmiş kısa ve uzun vadeli kararlılığa sahip, dijital olarak kontrol edilen yüksek performanslı bir FM MEMS dönüölçer sistemini sunmaktadır. Dijital dönüölçer sistemi, basitleştirilmiş elektronik donanım, küçük boyut, düşük güç ve farklı çalışma koşulları için kolay konfigürasyon için programlama ile artırılmış esneklik, gerçek zamanlı gelişmiş kalibrasyon ve kapsamlı test edilebilirlik gibi bir dizi avantaja sahiptir. Sistem, literatürde yüksek güçlü FPGA'lar ile uygulanan FM MEMS dönüölçer sistemlerinin aksine düşük güçlü bir mikrodenetleyici ile gerçeklenmiştir ve ticari yüksek performanslı MEMS dönüölçerler ile karşılaştırılabilir boyutta kompakt bir sensör paketine sığdırılması ile ticarileştirilmiş bir ürün olarak sunulabilmektedir.

Sistem, 8 adet dijital kontrol döngüsü için 75 kHz'den daha yüksek dijital kontrol döngüsü hızları gerektiren yaklaşık 7,5 kHz mekanik rezonans frekansına sahip bir MEMS dönüölçer için geliştirilmiştir. Bu zorlu dijital kontrol döngüsü hızlarına, donanım hızlandırıcıları ve kayıt düzeyinde programlama yöntemleri kullanılarak ulaşılabilmektedir. En kritik dijital kontrol döngüsü, FM çıkışının frekans okuması için kullanılan PLL döngüsüdür ve bu döngü, offset kararsızlığını geliştiren Lissajous FM yönteminin uygulanması için gerekli olan 100Hz'den daha büyük bir

ölçüm bant genişliği elde etmek için dikkatlice tasarlanmıştır. Literatürde ilk kez asimetrik MEMS jiroskop ile Lissajous FM yöntemi kullanılarak dönüölçerin açısal rastgele yürüyüş (ARW) performansı önemli ölçüde iyileştirildi; bu yaklaşım, birinci ve ikinci rezonans modlarının salınım genlik oranının 2500'e kadar çıkmasını sağlamaktadır (tamamen simetrik dönüölçer yapılarında 25'ten düşük değerlerin aksine), bu da 875Hz/(rad/sn) gibi rekor bir yüksek orantı katsayısı vermektedir, literatürde FM MEMS dönüölçerler için bildirilenlerden 100 kat daha yüksek.

FM MEMS dönüölçer sisteminin performansı, 0,52°/saat/√Hz'lik bir ARW değeri ve 0,2°/saat'lik bir ofset kararsızlığı değeri sağlayacak şekilde ölçülür ve literatürde bildirilen en iyi FM MEMS jiroskop sisteminin(yüksek güçlü ve hantal bir FPGA kartı ile geliştirilen) her bir değeri için yaklaşık 6 kat daha iyi performans göstermektedir.

Anahtar Kelimeler: FM MEMS Dönüölçer, Dijital kontrol

To My Family

ACKNOWLEDGMENTS

I would like to thank to my thesis advisor Prof. Dr. Tayfun Akın for their guidance, advice, criticism, encouragements and insight throughout the research. It is a great opportunity for me to make research together with him.

I would like to thank Prof. Dr. Haluk Külah and Assoc. Prof. Dr. Kıvanç Azgın for their comments and suggestions during the development of this thesis

Special thanks to Dr. Said Emre Alper and Hasan Doğan GAVCAR for sharing their deep knowledge and experiences in all phases of this research, and also for their friendship.

I would like to express my gratitude to Dr. M. Mert Torunbalcı, Dr. Burak Eminoğlu, Murat Yağcı, Selçuk Keskin, Evren Erdil, Dr. Mustafa Yıldırım, Adem Saraç for their supportive friendship throughout this thesis process.

I would like to thank to Mikrosistemler staff for their helps during the board manufacturing and test phases of this study, especially to İsmail Gökşen. I also would like to thank all members of the METU-MEMS family for providing a nice research environment.

I would like to express my deepest gratitude to my wife Lamia for her endless patience and continuous encouragement.

TABLE OF CONTENTS

LIST OF TABLES

TABLES

LIST OF FIGURES

FIGURES

CHAPTER 1

INTRODUCTION

The gyroscope is a critical component in a wide range of high-end industrial applications, from automotive to military. It is foreseeable that future inertial navigation and flight control markets will depend more and more on MEMS gyroscopes. These applications' requirements can be met by introducing customized control loops and enhancing their performance. The majority of MEMS gyroscopes are Coriolis vibrating gyroscopes, which operate in the amplitude modulated (AM) operational mode. Standard amplitude-modulated (AM) readout has made significant advancements in terms of angle random walk (ARW) and bias instability by improving parametric amplification, mode matching, sensor mechanical quality factor, and other technologies. However, the long-term stability for zero rate output and scale factor has proven challenging for the development of AM gyroscopes[1]. These error terms mainly occurred by quadrature coupling, an-isodamping, and very long signal chain in the AM gyroscope readout. However, an alternate operational mode of the vibratory gyroscope based on its frequency modulation (FM) effect has recently gained increasing attention to eliminate the error terms easily and effectively.

This chapter begins with a brief overview of the evolution of MEMS gyroscopes prior to the present attempts for new and improved gyroscope devices and concludes with performance standards and error sources. The subsequent chapter of this dissertation concentrate on the FM gyroscope's theory, implementation, and test results.

1.1 Overview of MEMS Gyroscopes

The earliest micromachined gyroscope research began in the early 1900s with quartz gyroscopes, however quartz-based techniques are not suited for semiconductor fabrication technology. This issue was resolved in 1991 by the Charles Stark Draper Laboratory, created a gyroscope that can be produced using semiconductor fabrication techniques, has a dual gimbal structure with a vertical bar, and has a resolution of 1° sec in a 1 Hz measuring bandwidth. [2]. Different types of gyroscopes appeared in the years that followed, including the piezoelectric vibrating gyroscope, MOMES gyroscope, micromachined vibrating gyroscope, atom gyroscope, thermal convective gyroscope, magnetic levitated gyroscope, and electrostatic levitated gyroscope[3]. These gyroscopes were made using several fabrication processes such as surface micromachining, wafer bonding, electroplating, bulk micromachining, and combination fabrication.

Over the years, the most often researched gyroscope type has been the micromachined vibrating gyroscope (MVG). The main focus of this category was the tuning fork vibratory gyroscope (TFG) with sense and drive electrodes. The current trend in MEMS is to downsize the complete system, including first mode, second mode, quadrature cancellation, and frequency matching control in a digital controller [4][5][6].

Alper [7] at METU MEMS has created a fully decoupled tuning fork gyroscope with higher performance that meets tactic level criteria. Tatar[8] builds and tests a completely decoupled tuning fork gyroscope with quadrature cancellation capabilities. Torunbalci [9][10][11] vacuum packages the investigated MEMS gyroscope. Eminoglu [12] researched CMOS readouts as well as the first systematization and modeling. Gavcar [13] cancels the acceleration sensitivity of the tuning fork gyroscope.

The first FM gyroscope investigations were undertaken by Seshia, who constructed a double-ended tuning fork gyroscope with the capacity to vary the elastic coefficient

using Coriolis force [14]. Moussa et al [15] created the first operational FM gyroscope that responds to changes in input angular velocity.

Kline et al. suggested a quadrature frequency modulated (QFM) mode FM gyroscope [16]. The two modes of the tuning fork gyroscope are orthogonally operated to modify the resonance frequency with regard to angular velocity. Furthermore, to eliminate the temperature effect, two QFM gyroscopes were operated with 90° and -90° phase shifts.

To mitigate gyroscope long-term drift, Eminoglu et al. presented an indexed FM gyroscope in which the phase difference between two resonant modes is regularly changed between +90° and -90°. Inversely, the IFM gyroscope's auto-zeroing rate limits the system bandwidth. [1].

Another option for canceling temperature dependency is to build an FM gyroscope using the Lissajous frequency-modulated mechanism, which continuously reverses the modes. This is accomplished by introducing some frequency difference between the modes[17]. As a result, the proof mass moves in a Lissajous pattern as shown in Figure 1.1, and the vibration phase difference between the two modes continuously varies from 0° to 360°. The LFM gyroscope modifies the resonance frequency of the two gyroscope working modes by modulating the angular rate to the mode separation frequency. Phase-sensitive demodulation of the two working mode frequencies followed by filtering can be used to determine the external angular rate. The output of the LFM gyroscope is unaffected by the temperature-dependent mode natural resonance frequency, in contrast to the QFM gyroscope. The LFM gyroscope benefits more from temperature stability of zero rate output as a result.

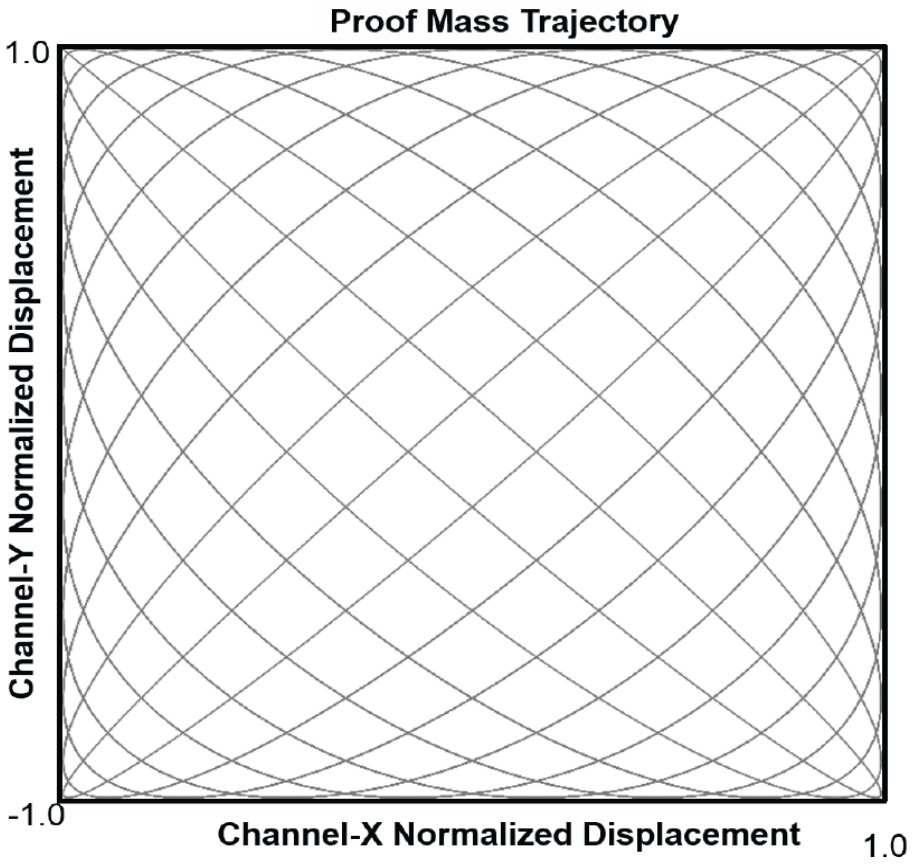

Figure 1.1. A Lissajous pattern is produced by the proof mass's trajectory when the x- and y-axis oscillators operate at various frequencies[16].

FM gyroscopes lock their vibration frequency to the resonance frequency of the mode, which is frequently done using self-oscillation [18]. In addition to the self-oscillation method, PLL can be used to maintain resonance [19]. If digital PLL is used to track the gyroscope resonance frequency, which can then be used directly for subsequent signal processing to obtain the angular rate information, eliminating the need for specialized frequency readout circuits, PLL can also be used as an optional excitation method for FM gyroscopes. The digital PLL system works with both AM and FM modes, so no additional interface circuitry is required.

1.2 Micromachined Vibratory Gyroscope and Performance Specifications

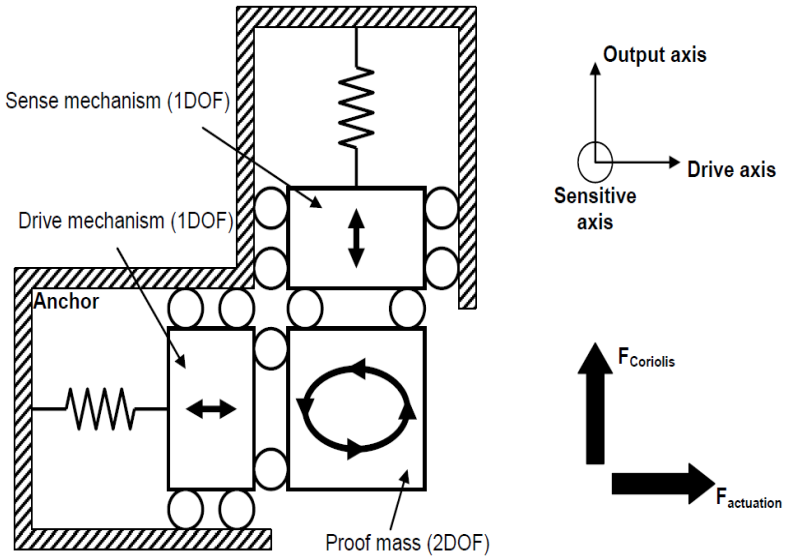

Figure 1.2. 2-DOF fully decoupled MEMS gyroscope structure[7].

As shown in Figure 1.2, MEMS gyroscopes are often built as double-ended tuning forks with a resonator that has two degrees of freedom (DOF). Shuttle frames with a 1-DOF and a 2-DOF proof mass make up this resonator. The total structure can simply be thought of as two discrete connected resonators traveling in orthogonal directions (x- and y- axis).

An inertial navigation system's gyroscope performance requirements are fairly demanding. Analysis and effective solution of the gyroscope's error sources are necessary to achieve the desired performance parameters.

The most important gyroscope error source for navigation systems is the bias error caused by undesired coupling forces between the resonators. There are three main undesired coupling mechanisms which results bias error in MEMS gyroscopes.

The first is quadrature coupling between two mechanically connected resonators, which is typically caused by manufacturing defects in spring and transduction imbalances. Because the quadrature error has a 90° phase difference with Coriolis,

it may be eliminated by synchronous demodulation. Any phase delay introduced into the loop, on the other hand, causes leakage and degrades the rate signal. To reduce the phase delay, the electronics' bandwidth is kept high by sacrificing power consumption.

The other error source is an-isodamping, which is in phase with Coriolis force and cannot be distinguished from the rate input as in the quadrature case. The answer is to improve the quality factor to reduce the fluidic coupling-related an-isodamping. However, if the MEMS structure is totally symmetric in both channels, this error can also be negated by alternating the channels in each other like auto-zeroing opamps.

Due to the misalignment and imbalance of the force electrodes caused by fabrication imperfections, force coupling error is the final source of bias error generation. The applied forces on these electrodes created in-phase error with Coriolis force. The first solution for this is to design the fully decoupled MEMS structure as in Figure 1.2. The residual force coupling can be cancelled by applying a perturbation signal on the drive electrodes[20].

The scale factor error is the second most common source of gyroscope inaccuracy in navigation systems. For AM gyroscopes, scale factor is often not as excellent as bias stability; nevertheless, for slowly rotating systems, scale factor inaccuracy does not degrade the system as much. However, today's systems are highly dynamic and rapid, necessitating very high scale factor stability in order to monitor the heading within a certain error margin.

To increase scale factor accuracy, all of the scale factor crucial parameters in the AM gyroscope must be precisely regulated; nevertheless, it is composed of multiple mechanical and electrical parts with varying characteristics. Scale factor may be assessed as frequency in the nature of angular rate to reduce scale factor related characteristics.

For very high dynamic systems, bandwidth of the MEMS gyroscope should be high enough to keep the error to some acceptable bound for the fastest possible input signal.

There are multiple performance grade gyroscopes based on the error rates of the MEMS gyroscope. These are classified as tactical-grade, rate-grade, and navigation-grade. Table 1.1 describes the performance standards for these three grades.

Table 1.1 Performance specifications for different grades of MEMS gyroscopes [21].

Parameter	Rate Grade	Tactical Grade	Inertial Grade
Angle Random Walk, $^0/\sqrt{hr}$	>0.5	0.5-0.05	<0.001
Bias Instability, $^0/hr$	10-1000	0.1-10	<0.01
Scale Factor Linearity, %	0.1-1	0.01-0.1	<0.001
Measurement Range, $^0/sec$	50-10000	>500	>400

1.3 The Studied Gyroscope

In this thesis, a digitally controlled FM MEMS gyroscope based on a microcontroller is implemented using a completely decoupled double ended tuning fork MEMS gyroscope. Although the drive and sensing modes of this gyroscope are not symmetric, the resonance frequencies of these modes were created to be able to electronically match them.

1.4 Research Objectives and Thesis Organization

The main objective of this thesis research is to design and implement the readout electronics of the Lissajous FM MEMS gyroscope with digital controller, as well as to improve the noise performance of the system through phase noise theory and testing. The main goals of this study can be listed in the following way:

1. The general theory of tuning fork gyroscopes should be investigated for AM and FM operation modes. The performance of gyroscope systems is strongly dependent on the operation principle and an effective examination of the theory behind the operation.
2. To build an oscillating system, the performance characteristics must be identified using oscillator theory. The performance of an oscillator is related to its phase noise performance. Calculations of phase noise for a standard MEMS oscillator and a PLL-operated MEMS oscillator should be performed.
3. The digital implementation of the FM gyroscope necessitates a large number of resources from the digital controller. The system's design and implementation should be done carefully in order to make the best use of the resources and keep the current consumption below that of commercialized tactical grade gyroscopes.

The thesis is organized as follows, and the contents of the succeeding chapters are as follows:

Chapter 2 examines in depth the tuning fork MEMS gyroscope following the derivation of the fictitious force. In addition, methods for mode-matching are presented.

Chapter 3 presents the derivation of coupled oscillators with two degrees of freedom. This derivation is used to characterize the frequency modulated gyroscope's transfer functions. After that, the operation and benefits of the Lissajous FM gyroscope are discussed.

Chapter 4 describes the oscillator's theory. Next, the phase noise derivations for linear and nonlinear operations are provided. Calculation of phase noise for the PLL-inserted closed loop oscillator is performed for use in performance analysis.

Chapter 5 The implementation of the digitally controlled FM gyroscope is presented. The design of digital PLL within this controller is also described in detail, along with the design procedures. In addition, the rate noise is calculated by determining the phase noises of the resonators and the scale factor of the Lissajous FM gyroscope.

CHAPTER 2

MEMS VIBRATORY GYROSCOPE

This thesis focuses on the application of the micromachined vibratory rate gyroscope. In this chapter, the theory underlying the MEMS vibratory gyroscope is discussed and the model of the gyroscope is derived. The mathematical formula of the Coriolis force generated on the gyroscope is described in Section 2.1. The sections 2.2 and 2.3 provide a comprehensive examination of the first and second modes, respectively. Section 2.5 describes the electronegative spring softening effect used to change the resonance frequency of the second mode. Section 2.6 describes the mode-matching approach. Finally, Section 2.7 presents a chapter overview.

2.1 The Coriolis Force

This fictitious force can only be theoretically calculated through the use of reference frames that are not inertial. A mass with a position vector $x_A(t)$ that may be calculated in the inertial frame A using Figure 2.1. The expression $X_{AB}(t)$ is the definition of a non-inertial frame in relation to frame A, and the expression $x_B(t)$ is the definition of mass in this frame. The forces that are acting on this mass in relation to frame B are going to be calculated.

As seen in frame B, the mass is oriented as follows:

$$x_B = \sum_{j=1}^{3} x_j \, u_j \qquad 2.1$$

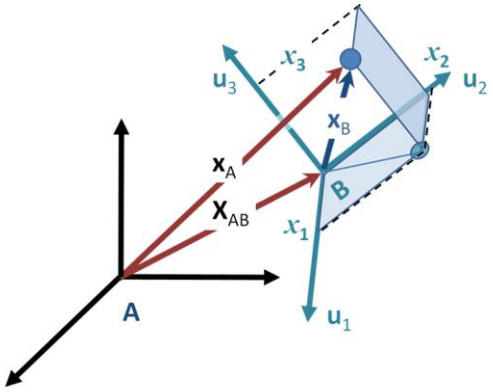

Figure 2.1. In accelerated frame B, an object that was once located at coordinate x_A in inertial frame A has now moved to coordinate x_B. At the coordinates X_{AB}, the start of frame B can be identified in frame A. The unit vectors that cross each of frame B's coordinate directions establish the orientation of the frame, u_j with j = 1, 2, and 3. The coordinates of the item in frame B are stated as follows when these axes are used: x_B = (x1, x2,x3).

In frame A, the mass is located as follows:

$$x_A = X_{AB} + \sum_{j=1}^{3} x_j \, u_j \qquad 2.2$$

By computing the derivative of x A in frame A, it is possible to find the velocity of the mass, as follows:

$$\frac{dx_A}{dt} = \frac{dX_{AB}}{dt} + \sum_{j=1}^{3} \frac{dx_j}{dt} u_j + \sum_{j=1}^{3} x_j \frac{du_j}{dt} \qquad 2.3$$

The acceleration of the mass can be calculated using the double derivative ofx_A using the following expression:

$$\frac{d^2 \mathrm{x_A}}{dt^2} = \mathrm{a}_{AB} + \mathrm{a}_B + 2\sum_{j=1}^{3} v_j \frac{d\mathrm{u}_j}{dt} + \sum_{j=1}^{3} x_j \frac{d^2 \mathrm{u}_j}{dt^2} \qquad 2.4$$

The first term in Equation 2.4 indicates frame B's acceleration in frame A. The true acceleration of the mass in frame B is the second term. As a result of the displacement of the frame B coordinate axes, an observer in frame B notices that the mass has three more acceleration terms. These fictitious acceleration components result from observers in frame B not recognizing frame B's non-inertial nature. The other two variables are related to the rotation of frame B, but the term $\mathrm{a_{AB}}$ is created by the acceleration of the frame B origin.

To determine the forces operating on this mass, multiply the acceleration terms by the mass.

$$\mathrm{F_A} = \mathrm{F_B} + m\mathrm{a_{AB}} + 2m\sum_{j=1}^{3} v_j \frac{d\mathrm{u}_j}{dt} + m\sum_{j=1}^{3} x_j \frac{d^2 \mathrm{u}_j}{dt^2} \qquad 2.5$$

Thus, Equation 2.6 can be used to describe the fictional force.

$$\mathrm{F_{fictitious}} = -m\mathrm{a_{AB}} - 2m\sum_{j=1}^{3} v_j \frac{d\mathrm{u}_j}{dt} - m\sum_{j=1}^{3} x_j \frac{d^2 \mathrm{u}_j}{dt^2} \qquad 2.6$$

The problem may then be addressed in frame B by considering the $\mathrm{F_{fictitious}}$ as an extra force.

Determining the perceived time rate of change of vectors is also necessary when frame B is defined as a rotating coordinate system, as in a gyroscope. A vector Ω whose magnitude is given by the below formula is used to describe the rotation of frame B.

$$|\Omega| = \frac{d\theta}{dt} = \omega(t) \tag{2.7}$$

All three frame B unit vectors have the same time derivative, which is

$$\frac{d\mathrm{u}_j(t)}{dt} = \Omega \times \mathrm{u}_j(t) \tag{2.8}$$

$$\frac{d^2\mathrm{u}_j}{dt^2} = \frac{d\Omega}{dt} \times \mathrm{u}_j + \Omega \times \left[\Omega \times \mathrm{u}_j(t)\right] \tag{2.9}$$

The acceleration that occurs in the translational direction can be eliminated by setting an $\mathrm{a}_{\mathrm{AB}} = 0$.

$$\mathrm{a}_A = \mathrm{a}_B + 2\Omega \times \mathrm{v}_\mathrm{B} + \frac{d\Omega}{d\mathrm{t}} \times \mathrm{x}_\mathrm{B} + \Omega \times (\Omega \times \mathrm{x}_\mathrm{B}) \tag{2.10}$$

Following is the complete mathematical equation for the fictitious force, which is a combination of Euler, the forces of centrifugal and Coriolis.

$$\mathrm{F}_{\mathrm{fictitious}} = -2m\Omega \times \mathrm{v}_\mathrm{B} - m\Omega \times (\Omega \times \mathrm{x}_\mathrm{B}) - m\frac{d\Omega}{d\mathrm{t}} \times \mathrm{x}_\mathrm{B} \tag{2.11}$$

It is now necessary to isolate the Coriolis force from the other terms. In the absence of a time-varying rate of rotation, some systems can cancel out the impact of centrifugal force, and the Euler force is assumed to be zero. Finally, we derived the gyroscope's most important notion for determining the rate of rotation in a non-inertial frame.

2.2 Expressions in First Resonant Mode

Equation 2.11 illustrates the development of the velocity term of the Coriolis force, v_B, the proof mass must oscillate along the first axis for an extended length of time. This velocity component is essential for a zero-rate output and constant scale factor due to gain mismatches. By precisely modeling the first mode dynamics, it is possible to maintain a constant v_B. Using Equations 2.12 and 2.14 as a starting point, Figure 2.2 shows a model of the spring-mass-damper system.

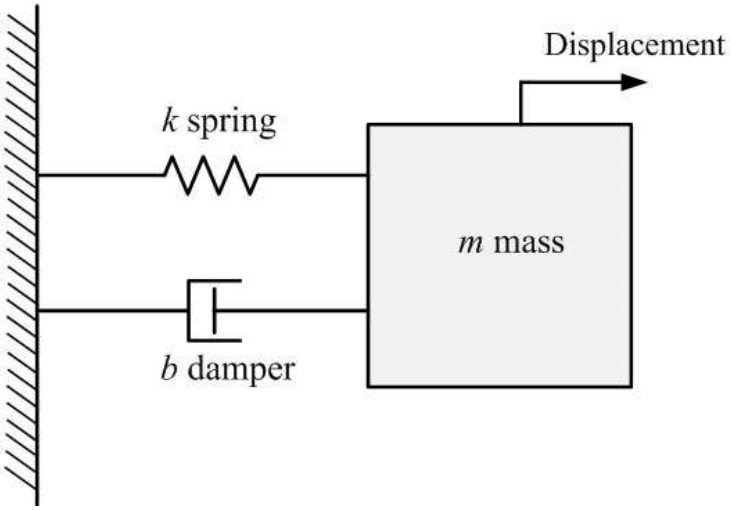

Figure 2.2. Spring Mass Damper System

The following system properties and displacement define the force delivered to the mechanical system:

$$F(s) = (m.s^2 + b.s + k).x \quad 2.12$$

Equations 2.13 and 2.14, which are derived from Equation 2.12, can be used to express the displacement and velocity, respectively.

$$\frac{X(s).s}{F(s)} = \frac{s}{m.s^2 + b.s + k} \quad 2.13$$

$$\frac{V(s)}{F(s)} = \frac{s}{m.s^2 + b.s + k} \quad 2.14$$

To describe the entire mechanical transfer function of the first mode, the processes that convert voltage to force and velocity to current must be stated and derived.

Variable overlap capacitors as in Figure 2.3 are used to accomplish the voltage-to-force conversion. This system is mathematically calculated from Equation 2.15 to Equation 2.17.

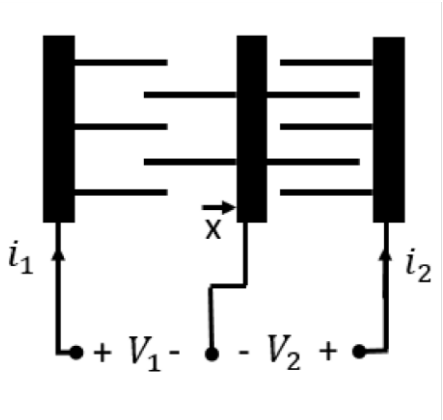

Figure 2.3. Varying overlap capacitor.

The energy equation for a capacitor serves as the starting point for this system's derivation. The force produced by the applied potential, which is shown in Equation 2.15, and continues with the derivation of that equation to determine that force, which is shown in Equation 2.16. On the other hand, the relationship between the applied potential and this force is not linear. This problem has been solved by adding additional DC potential to the applied potential, as this requirement has been mentioned. According to Equation 2.17, this potential will generate a linear force that is proportional to Vprof x Vac at the frequency of the AC potential that is being applied.

$$E = \frac{1}{2} C.V^2 \qquad 2.15$$

$$\frac{\partial E}{\partial x} = F = \frac{1}{2}.\frac{\partial C}{\partial x}.V^2 \qquad 2.16$$

$$F = \frac{1}{2}\frac{\partial C}{\partial x}(Vprof - Vac)^2$$
$$= \frac{1}{2}\frac{\partial C}{\partial x}((Vprof)^2 + (Vac)^2 - 2\,Vprof\,Vac) \qquad 2.17$$

The conversion of speed into current is yet another aspect of the first resonant mode. The speed of the mass is changed into a current by the utilization of variable overlap capacitors.

This conversion's derivation can be found by this fundamental Equation 2.18. With relation to the changing capacitance, Equation 2.19 gives an expression for this equation's time derivative.

$$Q = CV \tag{2.18}$$

$$I = \frac{\partial C}{\partial t}.V \tag{2.19}$$

In a gyroscope, $\frac{\partial C}{\partial x}$ is the most important parameter; therefore, $\frac{\partial C}{\partial t}$ is determined by $\frac{\partial C}{\partial x}.\frac{\partial x}{\partial t}$, as shown in Equation 2.20.

$$I = \frac{\partial C}{\partial x}.\frac{\partial x}{\partial t}.V \tag{2.20}$$

The whole transfer function of the driving mechanism can be defined using Equation 2.21, which incorporates Equations 2.14, 2.17, and 2.20. The equation that follows shows this.

$$\omega_D = \sqrt{\frac{k}{m}} \tag{2.21}$$

$$Q_D = \frac{\sqrt{k.m}}{b} \tag{2.22}$$

By modifying the transfer function from voltage to current using the aforementioned equations, a more understandable transfer function, represented by Equation 2.24, may be created.

$$\frac{I(s)}{Vac(s)} = -(\frac{\partial C}{\partial x}Vprof)^2 \frac{s}{m.\left(s^2 + \frac{\omega_D}{Q_D}.s + {\omega_D}^2\right)} \tag{2.23}$$

Equation 2.25, which includes ω_D, Q_D, and mechanical parameters, describes the $\frac{I(s)}{Vac(s)}$transfer function when the operating frequency is ω_D.

$$\frac{I(j\omega_D)}{Vac(j\omega_D)} = -(\frac{\partial C}{\partial x}Vprof)^2 \frac{Q_D}{m.\omega_D} \quad 2.24$$

At the frequency of mechanical resonance, $\frac{I}{Vac}$is directly proportional to Q_D, according to the final equation. Additionally, it shows that the system's displacement is at its maximum when the applied potential generates the smallest operational excitation force for a particular displacement amount. Furthermore, at the lowest level, the lowest excitation force couples mechanically and electrically to other systems.

2.3 Expressions in Second Resonant Mode

Dynamics in the first and second modes are very comparable. The actuation and sensing electrodes, on the other hand, are distinct from the first mode's electrodes. For actuation and sensing, capacitive electrodes with a varying gap are used instead. Due to the gyroscope's completely decoupled structure, the proof mass is the only component responsive to the fictitious force when producing the second mode dynamics. As a result, the second mode's dynamics can be represented as

$$\mathrm{F_{fictitious}} = -2m_{PM}\Omega_\mathrm{z} \times \mathrm{v_D} - m_\mathrm{PM}\Omega_\mathrm{z} \times (\Omega_\mathrm{z} \times \mathrm{x_D}) - m_{PM}\frac{d\Omega_\mathrm{z}}{d\mathrm{t}} \quad 2.25$$
$$\times \mathrm{x_D} = m_S\ddot{y}(t) + b_S\dot{y}(t) + k_S y(t)$$

The terms m_{PM} and m_S in Equation 2.25, respectively, stand for the proof mass and the mass of the second mode's electrodes combined.

Since the influence of centrifugal force may be countered by various systems, the $\mathrm{F_{fictitious}}$ can be taken to equal the sum of the Coriolis and Euler forces. With these changes, Equation 2.25 can be represented as Equation 2.26.

$$-2m_{PM}\Omega_z \times v_D - m_{PM}\frac{d\Omega_z}{dt} \times x_D = m_S\ddot{y}(t) + b_S\dot{y}(t) + k_S y(t) \quad 2.26$$

Assume an angular rate input that varies with time and a first mode displacement that varies with time as follows:

$$x_D(t) = X_D \cos(w_D t) \quad 2.27$$

$$\Omega_z(t) = \Omega_z \cos(w_z t) \quad 2.28$$

When Equation 2.27 and Equation 2.28 are plugged into Equation 2.26, the fictitious second mode dynamics are represented by Equation 2.29.

$$\begin{aligned} m_{PM}\Omega_z X_D \left\{ \left(w_D + \frac{w_z}{2}\right) \sin(w_D + w_z)t \right. \\ \left. + \left(w_D - \frac{w_z}{2}\right) \sin(w_D - w_z)t \right\} \\ = m_S\ddot{y}(t) + b_S\dot{y}(t) + k_S y(t) \end{aligned} \quad 2.29$$

Equations 2.30 and 2.31 show that there are two portions to the Coriolis force is along gyroscope's second mode, and they are equally spaced in the frequency domain with respect to the resonance frequency of the first mode, w_D. The amplitudes of these components can be expressed as

$$Y(w_D + w_z) = \frac{\frac{m_{PM}}{m_S} X_D \Omega_z \left(w_D + \frac{w_z}{2}\right)}{(w_s^2 - (w_D + w_z)^2) + j\frac{w_S}{Q_S}(w_D + w_z)} \qquad 2.30$$

$$Y(w_D - w_z) = \frac{\frac{m_{PM}}{m_S} X_D \Omega_z \left(w_D - \frac{w_z}{2}\right)}{(w_s^2 - (w_D - w_z)^2) + j\frac{w_S}{Q_S}(w_D - w_z)} \qquad 2.31$$

The second mode of the gyroscope performs two different tasks depending on the distinction between the resonance frequencies of the first and second modes. The first is a mismatched operation characterized by a wide frequency separation between two modes. This operation's response can be expressed as:

$$Y(w_D - w_z) + Y(w_D + w_z) = \frac{X_D \Omega_z}{(\Delta w) + j\frac{w_S}{Q_S}} \frac{m_{PM}}{m_S} \qquad 2.32$$

Mode-matched operation describes the second functioning of the gyroscope in which the first and second modes' resonance frequencies are somewhat closer together. The response of this operation can be expressed as:

$$Y(w_D - w_z) + Y(w_D + w_z) = \frac{X_D \Omega_z}{j\frac{w_S}{Q_S}} \frac{m_{PM}}{m_S} \qquad 2.33$$

Equations 2.32 and 2.33 show that the second mode displacement is improved by the quality factor of the second mode's structure when the resonance frequencies of the gyroscope's first and second modes are matched. This is the idea behind enhancing

the sensitivity of a vibratory gyroscope to reduce the electrical noise, as the quality factors for micro-machined resonators may approach millions at vacuum.

To get the whole second mode transfer function, it is also necessary to describe the voltage to force and velocity to current conversions.

Varying capacitors are used to excite and detect the motion in the second mode shown in Figure 2.4. The derivation of the forces and current generated by these varying capacitors should start with in Equations 2.35.

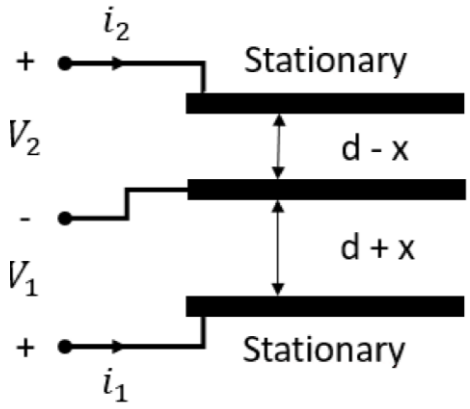

Figure 2.4. Varying gap capasitor.

$$\frac{dC}{dx} = \mp \frac{\text{Ɛ.h.l}}{(d \pm x)^2} \qquad 2.35$$

The following equation can be used to express the force produced by varying gap second mode electrodes.

$$FF = \frac{1}{2}.\frac{\partial C}{\partial x}.(Vprof - \mathrm{Vff})^2$$
$$= \frac{1}{2}.\frac{\partial C}{\partial x}.((Vprof^2 + \mathrm{Vff}^2) - 2.Vprof.\mathrm{Vff}) \quad 2.36$$

Equation 2.37 can be used to represent the current produced by varying gap second mode electrodes.

$$io = \frac{\partial C}{\partial x}.V_x.(Vprof - SP) \quad 2.37$$

2.4 Negative Spring Effect

This section will examine the notion of negative spring effect. There are two essential spring constants in a micromachined gyroscope. These defines the first and second mode's resonance frequency. Due to tolerances, the benefits of perfect matching cannot be reached when these springs are made using ordinary micromachining methods. However, mode matching may be accomplished by the use of negative spring effects at variable gap capacitive electrodes at second mode electrodes. Initially, the force created at the second mode electrodes will be examined, followed by the negative spring effect. The gyroscope frame is influenced by two forces. The mechanical force produced by mechanical springs is the primary force, whereas electrostatic forces are the secondary force. The corresponding expressions for these forces are Equation 2.38 and Equation 2.39.

$$F_{mech} = -k_{mech}.(x - x_0) \quad 2.38$$

$$F_{elec} = -\frac{1}{2}.\frac{A.\varepsilon}{x^2}.V^2 \quad 2.39$$

Since the mechanical frame is kept in its stable position by force feedback, the force equations can be linearized as in Equations 2.40 and 2.41.

Combining these two forces yields the result shown in Equation 2.42.

$$F_{mech} = \frac{dF_{mech}}{dy}.y = -k_{mech}.y \qquad 2.40$$

$$F_{elec} = \frac{dF_{elec}}{dy}.y = \frac{1}{2}.\frac{A.\varepsilon}{{y_0}^3}.y.V^2 \qquad 2.41$$

$$F_{mech} + F_{elec} = -k_{mech}.y + \frac{1}{2}.\frac{A.\varepsilon}{{y_0}^3}.y.V^2 = -k_{eff}.y \qquad 2.42$$

The only way to take advantage of the spring softening effect is to alter the applied DC voltage on the variable gap electrodes as shown in Equation 2.43. This will lower the effective resonance frequency of the mechanical system.

$$\omega_s = \sqrt{\frac{k_{eff}}{m}} = \sqrt{\frac{k_{mech} - \frac{1}{2}.\frac{A.\varepsilon}{{y_0}^3}.V^2}{m}} \qquad 2.43$$

2.5 Quadrature Offset

The coupling of the first mode displacement onto the second mode results in quadrature offset. Manufacturing tolerances cause this coupling, but this quadrature offset signal is the Coriolis signal with a 90° phase shift. Phase sensitive demodulation is the primary technique for canceling this offset, however phase errors

and the environmental error result in MEMS gyroscopes with reduced performance. In addition to the modulation technique, several approaches were created. The electrostatic quadrature reduction technique is the most efficient approach. Figure 2.5 shows the implementation structure of this offset reduction approach with a few electrodes.

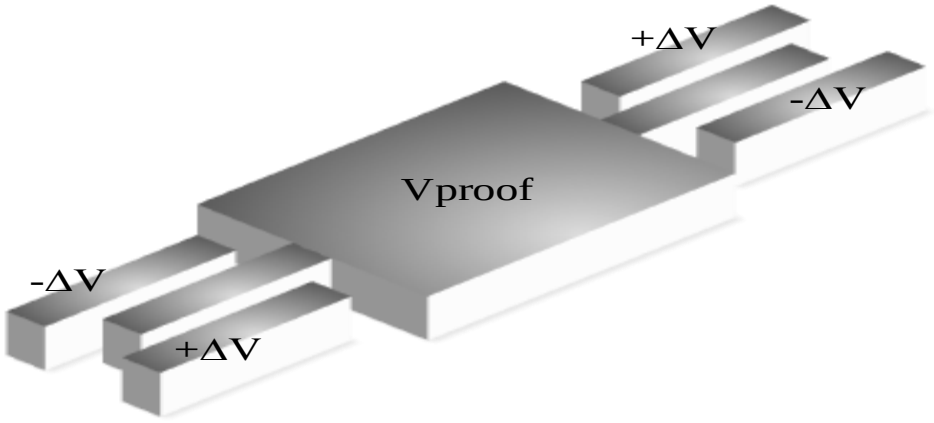

Figure 2.5. Structure of an electrostatic quadrature offset cancellation electrode.

In Figure 2.5, the proof mass moves along the x-axis. This motion causes a force in the y direction on the proof mass, which can be represented by Equation 2.44.

$$F_y = \frac{1}{2}.\frac{dC}{dy}.V^2 \qquad 2.44$$

Figure 2.5 depicts four capacitors that produce a force that is in phase with the quadrature offset and can be used as a suppression force.

$$
\begin{aligned}
F_y &= F_{quad_{cancel}} \\
&= \frac{1}{2}.\frac{\varepsilon.(L-X).h}{(y_0-y)^2}.(V_{DC}+\Delta V)^2 \\
&-\frac{1}{2}.\frac{\varepsilon.(L-X).h}{(y_0+y)^2}.(V_{DC}-\Delta V)^2 \\
&+\frac{1}{2}.\frac{\varepsilon.(L+X).h}{(y_0-y)^2}.(V_{DC}-\Delta V)^2 \\
&-\frac{1}{2}.\frac{\varepsilon.(L+X).h}{(y_0+y)^2}.(V_{DC}+\Delta V)^2
\end{aligned}
\qquad 2.45
$$

Equation 2.46 shows how to adjust the previous quadrature cancellation force equation for a tiny y-direction change.

$$
F_y = F_{quad_{cancel}} = -\frac{4.\mathcal{E}.V_{DC}.\Delta V.X.h}{{y_0}^2} \qquad 2.46
$$

In conclusion, only DC voltage was used to produce this AC force.

2.6 Mode Matching

MEMS gyroscopes have been used in tactical implementations where light weight and small size are critical. MEMS gyroscope performance, on the other hand, nearly met the requirements for navigation level applications. MEMS gyroscopes often meet these requirements by incorporating unique control loops that boost the noise performance of the device. It is known that the noise performance of a MEMS gyroscope is enhanced by matching the resonance frequencies of the first and second modes. In addition to mechanical Brownian noise, electrical noise is present in gyroscope systems. Usually, electrical noise rather than mechanical noise is what limits the performance of high-performance gyroscope systems. The first and second modes' specified mode matching boosts both the mechanical signal and the signal-

to-electrical noise ratio, enhancing the performance of the electrical noise restricted gyroscope system to meet navigation level criteria.

In a MEMS gyroscope system, rate information is obtained by the Coriolis effect coupling of the displacement of the first mode to the mass of the second mode. The coupling force is in phase with the first mode's motion, but the second mode signal will only receive this force if the first and second modes' resonance frequencies are within a certain range. The second mode signal is the first mode signal's 90 degree phase-shifted counterpart when the second mode's resonance frequency exceeds the first mode's resonance frequency. When the mode is matched, the modulation process is distinct because of a shift in the transfer function of the mechanical gyroscope's underlying mechanism. The rate information is obtained in a mode-matched scenario by modulating the second mode signal with the first mode signal. The signal-to-noise ratio is better than in the mismatched case because of mode-matching.

Implementing the mode-matching for high Q sensors, which require a frequency mismatch of less than a fraction of a hertz (Hz), is not an easy task, since manufacturing limitations place a limit on how near these frequencies can be consistently manufactured. Unfortunately, post-fabrication and once-off tuning approaches [26], [27] fall short of this criterion because they do not account for temperature and age-dependent fluctuations. While out-of-band pilot tones [29] and perturbation-based extremum seeking [28] are two methods that have been investigated for satisfying the continuity of mode matching, in both of them the perturbation signal is not fully decoupled from the angular rate control loop, requiring a frequency that is greater than 10 times the bandwidth of the angular rate control loop and leading to a significant loss of mechanical gain for the sensor in the mode-matching control loop. By including an AC signal in the quadrature control loop and observing the phase relationships between this signal and the signal from

the first mode, it is suggested that a different automated mode-matching system may be put into practice [30].

2.7 Conclusion

This chapter provided a comprehensive investigation of the fictional Coriolis Force and the modeling of the MEMS gyroscope. The MEMS gyroscope's capacitive actuation and sensing mechanisms are also described. In relation to the resonance frequency, the mode-matching mechanism, the electrostatic spring softening action, is thoroughly discussed. The mechanism for quadrature cancellation is then studied. Finally, the mode-matching system and its benefits are described, followed by the literature.

CHAPTER 3

FM GYROSCOPE

The operation of a FM gyroscope is depended on the modulation of resonance frequency by the angular rate [13]. Measurements of frequencies using a stable reference clock can acquire this frequency modulation. This ratio-metric readout naturally has less sensor parameter dependency, which reduces error terms in the bias and scale factor [12], because angular rate is itself a frequency.

While the first channel acts as an oscillator in traditional AM gyroscopes, the second channel serves merely as a sensory element. Nonetheless, with FM gyroscopes, both axes serve as oscillators. Comparing the online mode matching of FM and AM gyroscopes reveals that the online mode matching of FM gyroscopes is easier.

MEMS Rate gyroscopes have proven challenging to design mode-matching loops for. With AM gyroscopes, it's difficult to directly see the natural frequency since, at zero rate, the energy in the sensing mode is zero. To monitor the sense-axis dynamics off-resonance, pilot tones have been utilized, although they provide only a moderate degree of mode-matching frequency precision [14]. An alternative automatic mode-matching method is possible by incorporating an AC signal into the quadrature control loop and watching the phase connections between this signal and the driving signal [30]. However, this mode matching is also insufficient for matching the frequency of an extremely high Q resonator.

The FM gyroscope [15] is able to solve these issues since it can keep oscillating along all two of its axes. The FM gyroscope scale factor is proven to be independent of the mechanical damping and electromechanical coupling characteristics of the MEMS device, making mode-matching a simple task to do.

The dynamics of coupled oscillators acting as a gyroscope are explored in this chapter.

3.1 2 DOF Gyroscope

Below is a description of the electro-mechanical matrices for a 2-DOF coupled oscillators.

M as a mass matrix:

$$M = \begin{bmatrix} m_{xx} & 0 \\ 0 & m_{yy} \end{bmatrix} \quad 3.1$$

B as a damping matrix:

$$B = \begin{bmatrix} b_{xx} & b_{xy} \\ b_{yx} & b_{yy} \end{bmatrix} \quad 3.2$$

K as a spring matrix:

$$K = \begin{bmatrix} k_{xx} + k_{x_{tune}} & k_{xy} \\ k_{yx} & k_{yy} + k_{y_{tune}} \end{bmatrix} \quad 3.3$$

O as a rate matrix:

$$O = \begin{bmatrix} 0 & 2m\Omega\alpha_z \\ -2m\Omega\alpha_z & 0 \end{bmatrix} \quad 3.4$$

q as a position vector:

$$q = \begin{bmatrix} x \\ y \end{bmatrix} \tag{3.5}$$

F as a force matrix

$$F = \begin{bmatrix} F_{xv}\dfrac{\dot{x}}{V_x} + F_{xd}\dfrac{x}{A_x} \\ F_{yv}\dfrac{\dot{y}}{V_y} + F_{yd}\dfrac{y}{A_y} \end{bmatrix} \tag{3.6}$$

Where V_x, A_x, V_y, and A_y are the oscilation magnitudes for the displacement and velocity of the device.

The matrix form of the motion equations is expressed as:

$$F = M\ddot{q} + (B + O)\dot{q} + Kq \tag{3.7}$$

The equations of motion shown below can be obtained by importing Equations 3.1 through 3.6 into Equation 3.7.

$$m_{xx}\ddot{x} + \left(b_{xx} - \frac{F_{xv}}{V_x}\right)\dot{x} + \left(k_{xx} - \frac{F_{xd}}{A_x} + k_{x_{tune}}\right) + k_{xy}y + \left(b_{xy} + 2m\Omega\alpha_z\right)\dot{y} = 0 \tag{3.8}$$

$$m_{yy}\ddot{y} + \left(b_{yy} - \frac{F_{yv}}{V_y}\right)\dot{y} + \left(k_{yy} - \frac{F_{yd}}{A_y} + k_{y_{tune}}\right) + k_{yx}x + \left(b_{yx} - 2m\Omega\alpha_z\right)\dot{x} = 0 \quad (3.9)$$

As can be observed, these coupled forces have the ability to modify the effective damping and spring constant. The damping is modulated if it is in-phase with the velocity. The stiffness is modulated, if the coupled force and displacement are in phase.

By using normalized displacement and velocity components for any conceivable phase difference between the x and y channel displacement $\emptyset_{xy}$, we may decompose the coupling forces into the displacement and velocity components of the corresponding oscillator.

$$y = x\frac{A_y}{A_x}\cos(\emptyset_{yx}) + \dot{x}\frac{A_y}{V_x}\sin(\emptyset_{yx}) \quad (3.10)$$

$$\dot{y} = \dot{x}\frac{V_y}{V_x}\cos(\emptyset_{yx}) - x\frac{V_y}{A_x}\sin(\emptyset_{yx}) \quad (3.11)$$

$$x = y\frac{A_x}{A_y}\cos(\emptyset_{xy}) + \dot{y}\frac{A_x}{V_y}\sin(\emptyset_{xy}) \quad (3.12)$$

$$\dot{x} = \dot{y}\frac{V_x}{V_y}\cos(\emptyset_{xy}) - y\frac{V_x}{A_y}\sin(\emptyset_{xy}) \quad (3.13)$$

The effective damping and spring constant terms can be expressed by using the equations from 3.8 to 3.13 as below

$$k_{x_{eff}} = k_{xx} - \frac{F_{xd}}{A_x} + k_{x_{tune}} + \frac{A_y}{A_x} k_{xy} \cos(\emptyset_{xy}) + \frac{V_y}{A_x} b_{xy} \sin(\emptyset_{xy}) + 2m\Omega\alpha_z \frac{V_y}{A_x} \sin(\emptyset_{xy}) \quad 3.14$$

$$k_{y_{eff}} = k_{yy} - \frac{F_{yd}}{A_y} + k_{y_{tune}} + \frac{A_x}{A_y} k_{yx} \cos(\emptyset_{yx}) + \frac{V_x}{A_y} b_{yx} \sin(\emptyset_{yx}) - 2m\Omega\alpha_z \frac{V_x}{A_y} \sin(\emptyset_{yx}) \quad 3.15$$

$$b_{x_{eff}} = b_{xx} - \frac{F_{xv}}{V_x} + \frac{V_y}{V_x} b_{xy} \cos(\emptyset_{xy}) - \frac{A_y}{V_x} k_{xy} \sin(\emptyset_{xy}) + 2m\Omega\alpha_z \frac{V_y}{V_x} \cos(\emptyset_{xy}) \quad 3.16$$

$$b_{y_{eff}} = b_{yy} - \frac{F_{yv}}{V_y} + \frac{V_x}{V_y} b_{yx} \cos(\emptyset_{yx}) - \frac{A_x}{V_y} k_{yx} \sin(\emptyset_{yx}) + 2m\Omega\alpha_z \frac{V_x}{V_y} \cos(\emptyset_{yx}) \quad 3.17$$

There are 4 unknowns and 4 equations from 3.14 to 3.17. Force and oscillation frequencies can be calculated using these formulas.

At first, force calculations will be conducted. For a sustained oscillation, damping term should be zero. F_{xv} and F_{yv} can be found as follow:

$$F_{xv} = b_{xx}V_x + V_y b_{xy}\cos(\emptyset_{xy}) - A_y k_{xy}\sin(\emptyset_{xy}) + 2m\Omega\alpha_z V_y \cos(\emptyset_{xy}) \quad (3.18)$$

$$F_{yv} = b_{yy}V_y + V_x b_{yx}\cos(\emptyset_{yx}) - A_x k_{yx}\sin(\emptyset_{yx}) + 2m\Omega\alpha_z V_x \cos(\emptyset_{yx}) \quad (3.19)$$

In order to sense the frequency of the FM gyroscope, the instantaneous oscillation frequency should be found. This can be calculated by using the effective spring constant and mass of the resonan mode as $\sqrt{k_{eff}/m}$. It is well known that the mechanical spring constants control the nominal oscillation frequency. Thus, by expanding the Taylor series at the mechanical resonance frequencies, the instantaneous oscillation frequencies are obtained as

$$\omega_x = \sqrt{k_{x_{eff}}/m_{xx}} = \omega_{ox} + \frac{k_{x_{eff}}}{2m\omega_{ox}} \quad (3.20)$$

$$\omega_y = \sqrt{k_{y_{eff}}/m_{yy}} = \omega_{oy} + \frac{k_{y_{eff}}}{2m\omega_{oy}} \quad (3.21)$$

The following are the detailed expressions for the instantaneous frequencies:

$$\omega_x = \omega_{ox} - \frac{F_{xd}}{2mV_x} + \frac{k_{x_{tune}}}{2m\omega_{ox}} + \frac{A_y}{2mV_x} k_{xy} \cos(\emptyset_{xy}) + \frac{V_y}{2mV_x} b_{xy} \sin(\emptyset_{xy}) + \Omega\alpha_z \frac{V_y}{V_x} \sin(\emptyset_{xy}) \quad 3.22$$

$$\omega_y = \omega_{oy} - \frac{F_{yd}}{2mV_y} + \frac{k_{y_{tune}}}{2m\omega_{oy}} + \frac{A_x}{2mV_y} k_{yx} \cos(\emptyset_{yx}) + \frac{V_x}{2mV_y} b_{yx} \sin(\emptyset_{yx}) - \Omega\alpha_z \frac{V_x}{V_y} \sin(\emptyset_{yx}) \quad 3.23$$

When we sum ω_x and ω_y, we can obtain the rate related output from FM gyroscope. However, some of the offset signal caused by non-ideal coupling can be suppressed by changing the phase of the $\emptyset_{xy}$. We can get the rate-related output from the FM gyroscope by adding ω_x and ω_y. However, by manipulating the phase of the $\emptyset_{xy}$, signals resulting from the imperfect coupling may be eliminated. Additionally, as demonstrated by Equation 3.22 and Equation 3.23, there is a substantial benefit over force sensing because the angular gain determine the scale factor for frequency output.

If there is no active tuning on free running two resonant modes, we can obtain the scale factor expression including oscillation amplitude dependance as follow

$$SF = \alpha_z \frac{d\sum\omega}{d\Omega} = \alpha_z \left(\frac{V_y}{V_x} + \frac{V_x}{V_y} \right) \quad 3.24$$

Using one of the channels as a master resonator and locking the second resonator to it, then the scale scale factor will be $\alpha_z V_x/V_y$, as stated in the formula below.

$$SF = \alpha_z \left(\frac{V_x}{V_y} \right) \quad 3.25$$

3.2 Lissajous FM Gyroscope

Any variations to the resonance frequency appear as rate instability in a standard FM gyroscope operation. Mode-reversal approach can be employed to cancel these resonant frequency components. First and second modes are switched to cancel out any common terms in this mode reversal procedure, however the rate of change is constrained by the oscillator sustaining loop's slew rate. Another way to increase the rate of mode-reversal is to alternate between the states continuously without ever consciously draining the gyroscope of energy. This is possible if both axes are continuously excited while only the phase relationship between the two oscillations is controlled. A predetermined frequency split that also affects the phase at the mode-split frequency can be used to adjust the phase difference. Lissajous Frequency Modulated (LFM) Gyroscope is the name of this technique. Two structures in the (LFM) gyroscope with proof masses circling in opposite directions negate temperature-related changes in the resonant frequency. In its operation, the two oscillation modes are oscillated and locked with a digital PLL inside the loop. The PLLs inside the two oscillating loops provide the direct frequency reading from the oscillators. After we obtain the oscillation frequencies, frequency split is adjusted by tuning the prof mass of the second mode to pre-defined frequency.

The instantaneous frequencies of the two modes can be expressed as below:

$$\dot{\phi}_x = \omega_{ox} - \alpha_z \frac{V_y}{V_x} \Omega_z \sin \Delta\phi_{xy} \tag{3.26}$$

$$\dot{\phi}_y = \omega_{oy} - \alpha_z \frac{V_x}{V_y} \Omega_z \sin \Delta\phi_{xy} \tag{3.27}$$

The frequency sum gives the rate dependent out as in Equation below. However, this equation has very high DC component coming from the mechanical resonant frequencies.

$$\sum \dot{\phi}_{xy} = \omega_{ox} + \omega_{oy} - \left(\frac{V_y}{V_x} + \frac{V_x}{V_y}\right) \alpha_z \Omega_z \sin \Delta\phi_{xy} \tag{3.28}$$

In order to suppress the DC component of the sum of frequencies, very low cut-off frequency high pass filter is used. After filtering the signal, we have rate signal modulated by the phase difference between the modes.

This signal can be modulated with the sine of the phase difference to reveal rate information. In an analog PLL driven systems, the acquisition of the phase is difficult to obtain; but in the digital PLL, we can acquire the phase difference from the software. After doing the modulation we have obtained the signal below:

$$\sin \Delta\phi_{xy}\, h_{HPF} \sum \dot{\phi}_{xy} \approx -\frac{1}{2}\left(\frac{V_y}{V_x} + \frac{V_x}{V_y}\right) \alpha_z \Omega_z \left(1 - \cos 2\Delta\phi_{xy}\right) \tag{3.29}$$

Now, we have obtained the rate data with DC and $\cos 2\Delta\phi_{xy}$ components. At the modulator's output, a low pass filter can be used to suppress the image at $2\Delta\phi_{xy}$. Finally, we get the rate out from the frequency outputs as follow:

$$h_{LPF}\left(\sin \Delta\emptyset_{xy}\, h_{HPF} \sum \dot{\emptyset}_{xy}\right) \approx -\frac{1}{2}\left(\frac{V_y}{V_x}+\frac{V_x}{V_y}\right)\alpha_z \Omega_z \qquad (3.30)$$

Thus, in this equation, phase is the directly related with the velocity ratios and the angular gain. Therefore, we obtained a very short definition of the rate that has very low mechanical and electrical disturbances.

CHAPTER 4

PERFORMANCE ANALYSIS

Due to frequency output of FM gyroscope, phase noise dominates the major angular random walk (ARW) performance of the gyroscope. It is essential to determine the relative weights of various physical noise sources, since their effects on the overall performance of the system vary. Meantime, the combinations of these many sources will result in non-linear frequency jitter, which may degrade the overall performance of the system.

4.1 Oscillator

As illustrated in Figure 4.1, the most general definition of an oscillator is a closed loop of a non-linear circuit with frequency dependency subsystem. G(ω,A) is the block's transfer function, while A and ω are its amplitude and frequency.

If the circuit has a small bandwidth, the system changes into a harmonic type oscillating system having sinus shaped signal. At frequency ω_s, stable oscillations with an amplitude A_s are possible.

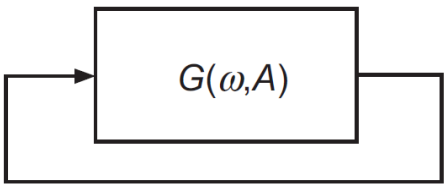

Figure 4.1. Oscillator generic representation

$$G(\omega_s, A_s)=1 \tag{4.1}$$

Nevertheless, this is only viable under two essential criteria. The first condition is the stability of the phase. [22]

$$\frac{d(argG)}{d\omega}|_{\omega_s,A_s} < 0 \tag{4.2}$$

If this condition is not satisfied, no periodic solution may be kept. The second need is amplitude stability.

$$\frac{d|G|}{dA}|_{\omega_s,A_s} < 0 \tag{4.3}$$

In this case, a nonlinearity in the circuit block is required to fix the amplitude of the oscillation.

Because every oscillator is a continuously changing system, it is vital to account for this aspect in order to appropriately explain phase noise. The time-variant model, in contrast to linear and time-invariant ones, can accurately measure phase noise by incorporating stationary and cyclostationary noise sources.

The two different forms of noise producers in a circuit are circuit noise and disturbance. Examples of the former include thermal noise, flicker noise, and shot noise. This model integrates earlier models as particular limiting circumstances and discusses in detail how random or deterministic sources, are affected into amplitude and phase noises.

4.2 Phase Noise in Linear Circuits

The amplitude and phase of an oscillator's output can be affected by noise in the circuit and device. However, most real oscillators must incorporate an amplitude control system. Because amplitude variations are often muffled, phase noise generally takes precedence.

The amplitude of an oscillator is accurately determined and is regulated by the circuit's nonlinearity. If there is an amplitude disturbance, the oscillator will reject it automatically.

The oscillation happens at a frequency where the loop gain is unity, which results in this. Non-compressive linearity's properties cause the loop multiplication to decrease and the oscillation amplitude to decrease as the amplitude rises.

Oscillator having phase shift has a viable correction. Due to the lack of "restoring force," the phase distortion continues if a disturbance causes the oscillator to shift phase.

To investigate the phase noise of an oscillator in a linear circuit subject to time-invariant noise sources, Leeson's classical approach [23] may be utilized. In a steady state of oscillation, the circuit model of the oscillator is shown in Figure 4.2.

The resonator's associated with motional resistance Rm is connected to a noise voltage with a $4kTR_m$ noise density. Spectral density $S_{V_n^2}$'s open loop real component of the method which enables during continuous oscillation, which is equal to R_m, may thus be connected to noise voltage V_n.

$$S_{V_n^2} = 4kT\gamma R_m \tag{4.4}$$

Where γ represents an excess factor of noise that is proportional to the circuit's individual noise contributions.

In a state of steady oscillation, the impedance Z_L generated by the resonator's movable components L_m and C_m, as well as the circuit's capacitance C_c, is the impedance required to load a noise voltage source with a spectral density of $4kTR_m(1+\gamma)$.

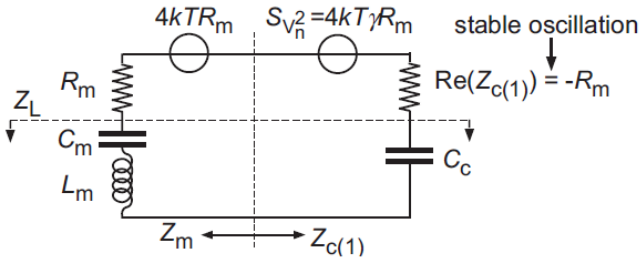

Figure 4.2. The circuit model of the oscillator in a steady state of oscillation[23].

The formula for steady oscillation's frequency is

$$\omega_s = 2\pi f_s = \frac{1}{\sqrt{L_m(C_m /\!/ C_c)}} \tag{4.5}$$

Consequently, one might write down the loading impedance for noise sources as

$$Z_L = j\omega_n L_m + \frac{1}{j\omega_n(C_m /\!/ C_c)} = j\omega_n L_m \frac{(\omega_n+\omega_s)(\omega_n-\omega_s)}{\omega_n^2} \tag{4.6}$$

where ω_n is the frequency at which noise is evaluated.

For very low frequency difference, the load impedance can be defined by

$$Z_L = 2j\omega L_m \frac{(\omega_n - \omega_s)}{\omega} = 2j\omega Q R_m \frac{(\omega_n - \omega_s)}{\omega} \tag{4.7}$$

The noise current I_{nL} flowing through the loop's power spectral density is then calculated.

$$S_{I_{nL}^2} = \frac{4kT(1+\gamma)R_m}{|Z_L|^2} = \frac{kT(1+\gamma)}{Q^2 R_m}\left(\frac{\omega}{\Delta\omega}\right)^2 \tag{4.8}$$

where $\Delta\omega$ is the difference between the stable oscillation frequency ω_s and the noise frequency ω_n

The oscillation (motional) current I_m is combined with this noise current. The associated complex phasors for a fundamental bandwidth df at an angular frequency ω are shown in Figure 4.3 at a certain time. The noise phasor's length, denoted by dI_n, is a random number with variance $S_{I_{nL}^2}$.

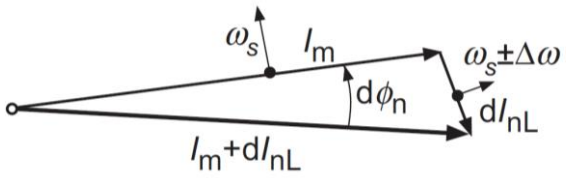

Figure 4.3. Elementary noise currents dI_{nL} and complex phasors of oscillation current I_m at a certain time.

dI_n has a component on both amplitude and phase noise. If we assume dI_n is totally white noise, then due to the equipartition theorem of thermodynamics, the powers of phase and amplitude noise are equal. Because of the automatic amplitude controllers in the oscillators, the oscillator's amplitude noise is eliminated, leaving only the remaining half of the $S_{I_{nL}^2}$ noise.

Considering that the noise current is small in comparison to the motional current, we can now evaluate the phase noise $\emptyset_n$.

$$S_{\emptyset_n^2} = \frac{\frac{1}{2} S_{I_{nL}^2}}{\left(\frac{|I_m|}{\sqrt{2}}\right)^2} = \frac{kT(1+\gamma)\omega^2}{Q^2 R_m |I_m|^2 \Delta\omega^2} \tag{4.9}$$

The power spectrum of phase noise is thus proportional to $\frac{1}{\Delta\omega^2}$. $S_{\varphi n}$ is inversely related to both the energy of the oscillation and the quality factor for a particular oscillation frequency.

The phase noise power spectrum is therefore inversely proportional to $\frac{1}{\Delta\omega^2}$. $S_{\emptyset_n^2}$ is inversely proportional to both the oscillation's energy and the quality factor for a certain oscillation frequency.

Figure 4.4 depicts a typical frequency spectrum from the oscillator of an FM gyroscope and its accompanying phase noise spectrum. The bias instability and resolution of the FM gyroscope are defined, respectively, by the frequency noise in the 1/f region and the white noise floor. These metrics may be examined using the three frequency spectrum areas.

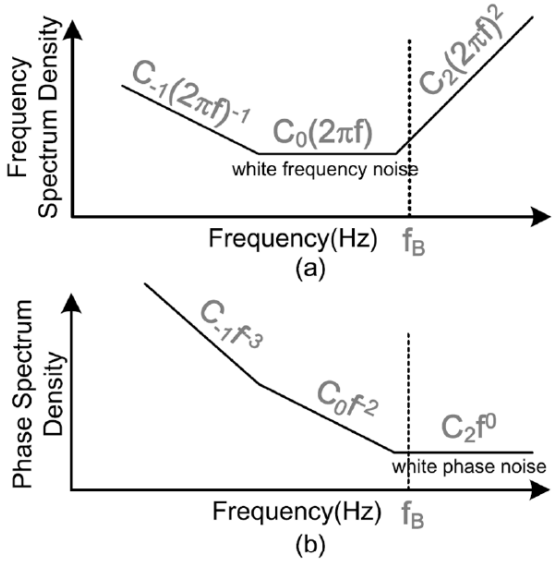

Figure 4.4. Frequency noise density of FM gyroscope's oscillator.

4.3 Phase Noise in Non-Linear Circuits

Numerous research [23], [24] have subsequently focused on phase and frequency variations. Although several models have been established for various kinds of oscillators, each model contains assumptions that are relevant to just a subset of oscillators. Most of these models are based on the linear time invariant system assumption, which leaves out the whole process by which electrical noise sources, including device noise, create phase noise. In specifically, they describe the up-conversion of low frequency noise sources, such as close-in phase noise using an empirical method. As reduced-order models, these models are likewise unable to accurately anticipate phase noise in long ring oscillators or oscillators with crucial singularities, such as delay elements.

Every oscillator is a regularly time-varying system, hence phase noise must be described in terms of the time-varying character of each oscillator. The time-variant model given here may accurately examine the effect of stationary and even cyclo-stationary noise sources on phase noise, in contrast to models that assume linear and time-invariance.

The circuit's noise sources can be classified into two categories: device noise and interfering noise. Thermal, flicker, and shot noise are examples of the first category, while substrate and supply noise are examples of the latter. The time-variant model describes the precise method by which random or deterministic spurious sources are turned into amplitude and phase changes.

This time-variant model predicts explicitly the connection between waveform shape and 1/f noise up conversion. Contrary to popular assumption, it will be shown that the $1/f^3$ corner of the phase noise spectrum is smaller than the 1/f noise corner of the oscillator's components by a factor defined by the symmetries of the waveform.

There is a significant distinction between the phase and amplitude responses of any actual oscillator, since an amplitude-limiting mechanism is required for steady oscillatory activity. The system state will eventually reach this trajectory, known as

a limit cycle, regardless of its initial condition. Nonetheless, any variation in the phase of the oscillation stays forever, with a current noise impulse resulting in a step shift in phase, as seen in Figure 4.5.

The phase shift makes the circuit nonlinear, and the noise generated by the active components turns into cyclostationary. Using the impulse sensitivity function (ISF) proposed by Hadjimiri and Lee [25], phase noise may then be investigated.

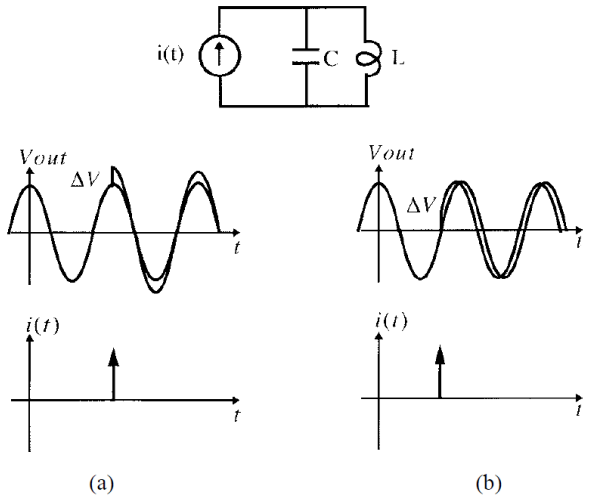

Figure 4.5. Time variant impulse effect on oscillator (a) Impulse injected at the peak, (b) impulse injected at the zero crossing [25].

An expression for the phase noise spectrum density due to the white noise voltage $V_n(t)$ with spectral density $S_{V_n^2}$ in this non-linear case is

$$S_{\emptyset_n^2} = \frac{\overline{\Gamma_v^2}\, S_{V_n^2}}{2(L_m|I_m|)^2\Delta\omega^2} \tag{4.10}$$

Using the effective impulse sensitivity function (ISF) Γ_v defined for the sinusoidal current $|I_m|\cos\emptyset$ by

$$\Gamma_v = -\sin\emptyset \cdot \alpha_v(\emptyset) \tag{4.11}$$

Spectrum density of phase noise $\frac{K_{\mathrm{f\,v}}}{\omega_n}$ from $\frac{1}{f}$ flicker noise voltage source:

$$S_{\emptyset_n^2} = \frac{\overline{\Gamma_v^2} \cdot K_{\mathrm{f\,v}}}{(L_m|I_m|)^2 \Delta\omega^3} \tag{4.12}$$

Thus, non-linearity in the oscillator heavily affects the $\frac{1}{f^3}$ region of the phase spectrum. However, in a FM gyroscope operated with Lissajous Pattern Method, $\frac{1}{f^3}$ region is eliminated by using chopping feature. Because of that, phase noise model in linear circuits model will be enough for the performance analysis.

As a result, the $\frac{1}{f^3}$ region of the phase spectrum is profoundly impacted by non-linearity in the oscillator. In contrast, the $\frac{1}{f^3}$ region is eliminated in a FM gyroscope that is controlled using the Lissajous Pattern Method thanks to the chopping function. Therefore, the performance analysis can be done using just the phase noise model in the linear circuits model.

4.4 Phase Noise Calculation for Oscillator with Analog Gain Control

Phase noise calculation of this type of oscillator can be done by modelling RLC circuit model as impedance around oscillation frequency. In Equation 4.13, the simplified base-band model was expressed.

The impedance of the MEMS resonator:

$$Z_L = 2j\omega L_m \frac{(\omega_n - \omega_s)}{\omega} = 2j\omega Q R_m \frac{(\omega_n - \omega_s)}{\omega} \tag{4.13}$$

The simplified circuit model of the linear oscillator with analog gain control can be seen at Figure 4.6. This circuit have the base-band model for the resonator, Preamplifier with a gain of Z_{pre} and an amplifier with a gain control as VGA.

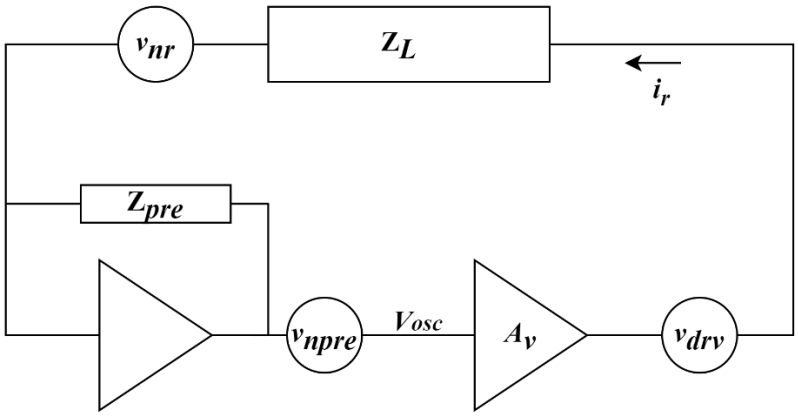

Figure 4.6. The simplified circuit model of the linear oscillator.

To create oscillations that are self-sustaining, the electrical resistance seen by the resonator must negate the motional resistance: $R_m = Z_{pre}A_v$. After defining the gains, circuit parameters and noise sources, the effects of the noises at the output can be calculated as follow:

$\grave{v}_{npre}$ *is t*he noise contribution of the v_{npre} at the output:

$$\grave{v}_{npre} = \frac{v_{npre}}{1 + \frac{R_m}{Z_{pre}}\frac{Z_{pre}}{Z_L}} = \frac{v_{npre}}{1 + \frac{R_m}{2QR_m\Delta\omega}} = \frac{v_{npre}}{1 + \frac{1}{2Q\Delta\omega}} \tag{4.14}$$

$\grave{v}_{ndrv}\ is\ t$he noise contribution of the v_{ndrv} at the output:

$$\grave{v}_{ndrv} = \frac{v_{ndrv}\ \frac{Z_{pre}}{Z_L}}{1+\frac{1}{2Q\Delta\omega}} = \frac{v_{ndrv}\ \frac{Z_{pre}}{2QR_m\Delta\omega}}{1+\frac{1}{2Q\Delta\omega}} = \frac{v_{ndrv}Z_{pre}}{2QR_m\Delta\omega\ + R_m} \tag{4.15}$$

$\grave{v}_{nr}\ is\ t$he noise contribution of the v_{nr} at the output:

$$\grave{v}_{nr} = \frac{v_{nr}\ \frac{Z_{pre}}{Z_L}}{1+\frac{1}{2Q\Delta\omega}} = \frac{v_{nr}Z_{pre}}{2QR_m\Delta\omega\ + R_m} = \frac{v_{nr}Z_{pre}}{2QR_m\Delta\omega\ + R_m} \tag{4.16}$$

The total noise at the output can be expressed below:

$$\begin{aligned} {v_{nosc}}^2 &= {\grave{v}_{nr}}^2 + {\grave{v}_{ndrv}}^2 + {\grave{v}_{npre}}^2 \\ &= \frac{\left(\frac{Z_{pre}}{R_m}\right)^2 ({v_{nr}}^2 + {v_{ndrv}}^2) + \left(2Q\Delta\omega\, v_{npre}\right)^2}{(1+\ 2Q\Delta\omega)^2} \end{aligned} \tag{4.17}$$

We can compute the phase noise $\emptyset_n$ assuming that the noise current is small relative to the motional current as in Equation 4.9. In this equation, half of the noise power contributes the phase noise, the other half contributes the amplitude noise. Therefore, the half the total noise power should be in the phase noise calculation. The spot noise at frequencies of $f_0 \pm \Delta f$, on the other hand, is what produces the phase noise at a frequency offset of Δf. This additional 3dB noise penalty, which is based on the assumption that noise is white around f_0, makes up for the prior 3dB drop. Consequently, it is easy to determine phase noise using the spot noise values of the noise sources.

However, spot noise at frequencies of $f_0 \pm \Delta f$ causes phase noise with a frequency offset of Δf. This is an additional 3dB noise increase, assuming white noise

surrounding f_0. Thus, the following formula can be used to determine phase noise from the spot noise values of the noise sources.

$$\emptyset_n^2 = \frac{{v_{nout}}^2}{{i_r}^2 {Z_{pre}}^2} = \frac{\left(\frac{1}{R_m}\right)^2 ({v_{nr}}^2 + {v_{ndrv}}^2) + \left(\frac{2Q\Delta\omega\, v_{npre}}{Z_{pre}}\right)^2}{{i_r}^2(1 + 2Q\Delta\omega)^2} \tag{4.18}$$

The output of the FM gyroscope is the frequency; Therefore, the frequency noise should be calculated from this phase noise. This can be accomplished by multiplying the phase noise with the $\Delta\omega$ which is the frequency mismatch used for rate modulation.

$$\omega_n^2 = \emptyset_n^2 \Delta\omega^2 = \frac{\left(\frac{\Delta\omega}{R_m}\right)^2 ({v_{nr}}^2 + {v_{ndrv}}^2) + \left(\frac{2Q\Delta\omega^2 v_{npre}}{Z_{pre}}\right)^2}{{i_r}^2(1 + 2Q\Delta\omega)^2} \tag{4.19}$$

At low frequency split $\Delta\omega$, noise is white and dominated by mechanical noises; but when the mode split is increased, frequency noise increases and this noise is dominated by electrical noise.

A linear relationship between preamplifier noise and mode-split is given by Equation 4.19. This performance is identical to that of standard AM gyroscopes. AM gyros are likewise related to the effects of Brownian noise and the expressions of feedback noise. If you want your system to perform as well as possible in terms of Brownian noise over a specific full-scale range, reducing mode-split and increasing motional current are both good places to start.

Rate-referred noise can easily be found by dividing the frequency noise with the SF which is $\alpha_z \left(\frac{V_y}{V_x} + \frac{V_x}{V_y}\right)$for FM gyroscope. The noise in dps/rt-Hz can be expressed as

$$\Omega_n\left[\frac{dps}{\sqrt{Hz}}\right] = \frac{\omega_n}{2\pi SF}360\frac{dps}{\sqrt{Hz}}$$

$$= \sqrt{\left(\frac{\left(\frac{\Delta\omega}{R_m}\right)^2({v_{nr}}^2 + {v_{ndrv}}^2) + \left(\frac{2Q\Delta\omega^2 v_{npre}}{Z_{pre}}\right)^2}{{i_r}^2(1 + 2Q\Delta\omega)^2}\right)}\frac{360}{2\pi}\frac{1}{\alpha_z\left(\frac{V_y}{V_x} + \frac{V_x}{V_y}\right)} \quad (4.20)$$

4.5 Phase Noise Calculation for Oscillator with Digital PLL

There are two distinct excitation techniques employed in gyroscope functioning, both of which serve to maintain the driving mode in a resonant state. Resonance can be kept running via PLL or the self-oscillation technique. Digital PLL may be utilized as an alternative excitation technique for FM gyroscopes by tracking the gyroscope's resonance frequency; this frequency can then be used in subsequent signal processing to determine the angular rate without the requirement for dedicated frequency readout circuitry. There is also no need for specialized interface circuitry between the AM and FM modes and the digital PLL solution.

Phase noise calculation of this type of oscillator can be done by modelling RLC circuit model as impedance around oscillation frequency as before.

The simplified circuit model of the oscillator with digital PLL can be constructed as in Figure 4.7.

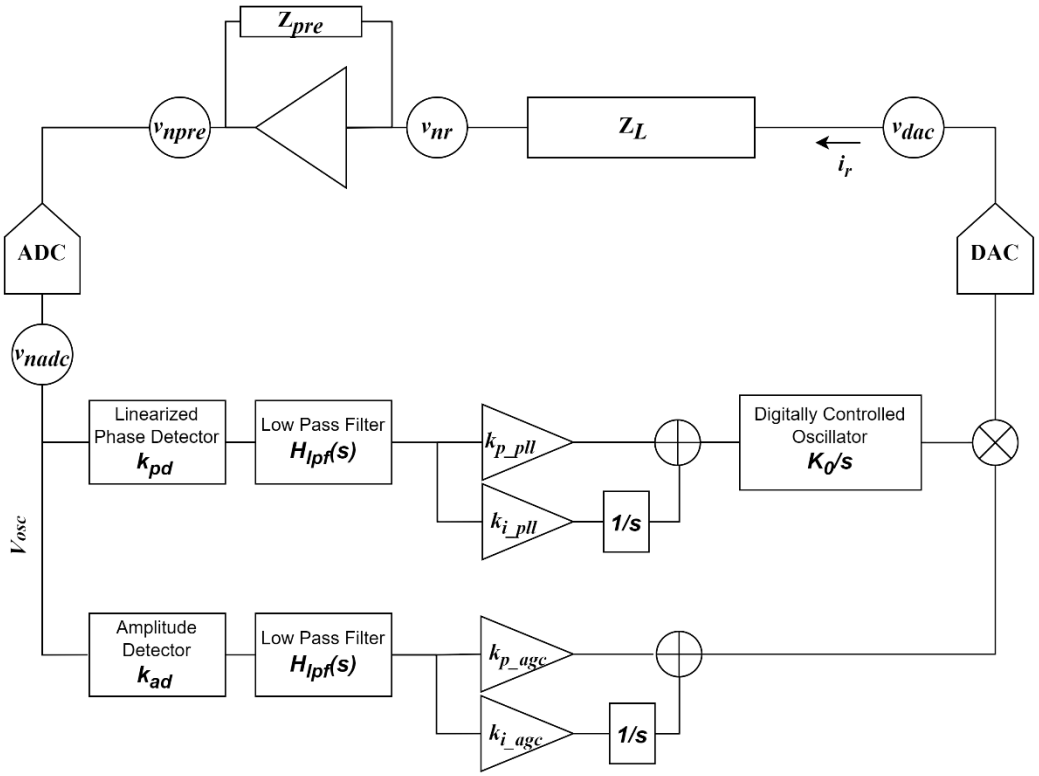

Figure 4.7. The simplified circuit model of the oscillator with digital PLL.

The phase noise of this digital oscillator is similar with the linear oscillator. However, there are some extra noise sources coming from the ADC and DAC. At first, the noise contribution of the noise sources should be calculated. After that, the noise shaping of the PLL will be calculated with the controller parameters of the PLL.

In order to sustain the oscillation, the gain of the automatic gain controller is same with the linear oscillator; because of that the total noise at the output of the ADC can be calculated as follow:

$$v_{nosc}{}^2 = \frac{\left(\frac{Z_{pre}}{R_m}\right)^2 (v_{nr}{}^2 + v_{ndrv}{}^2 + v_{ndac}{}^2) + (2Q\Delta\omega)^2 (v_{npre}{}^2 + v_{nadc}{}^2)}{(1 + 2Q\Delta\omega)^2} \quad (4.21)$$

Phase noise can thus be calculated from the spot noise values of the noise sources as follow.

$$\emptyset_n^2 = \frac{v_{nosc}{}^2}{i_r{}^2 Z_{pre}{}^2} = \frac{\left(\frac{1}{R_m}\right)^2 (v_{nr}{}^2 + v_{ndrv}{}^2 + v_{ndac}{}^2) + \left(\frac{2Q\Delta\omega}{Z_{pre}}\right)^2 (v_{npre}{}^2 + v_{nadc}{}^2)}{i_r{}^2 (1 + 2Q\Delta\omega)^2} \quad (4.22)$$

At this point, we have calculated the phase noise contribution at the input of the PLL. Then, we will calculate the noise shaping characteristics and the output phase and frequency noise of the PLL by using closed loop transfer function.

To calculate the transfer function of the PLL, PLL can be modelled as a linear closed loop system as in Figure 4.8. The details of the linearized model can be found at Chapter 5.

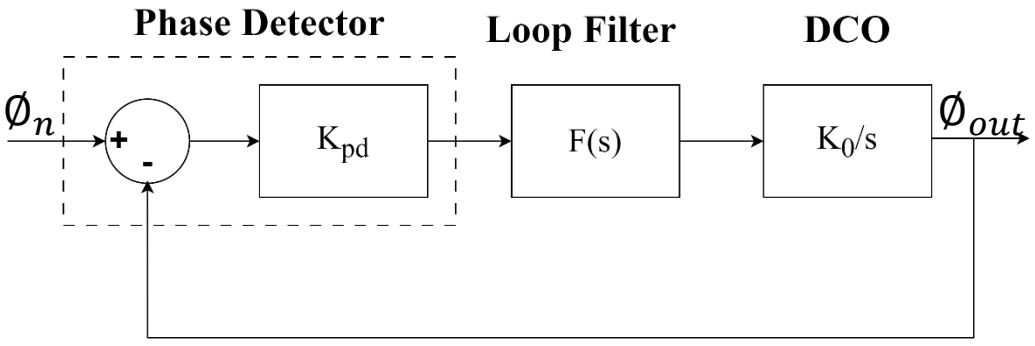

Figure 4.8. The linearized PLL model.

The phase noise transfer function can be calculated by using the closed loop transfer function as follow:

We assume the system is linear with regard to the phase relationship since both the noise input and the PLL output are phase signals and can be analyzed using the transfer function H(s). Furthermore, we will presume that the PLL is locked.

$$H(s) = \frac{\emptyset_{out}(s)}{\emptyset_n(s)} \tag{4.23}$$

As a result, H(s) is now a phase transfer function, and PLL is a phase-signal-controlling mechanism. Consequently, the following expression for the transfer function is expressed by fundamentals of control theory:

$$H(s) = \frac{K_{pd}F(s)K_0}{s + K_{pd}F(s)K_0} \tag{4.24}$$

The $\emptyset_{out}$ can be computed after we have the H(s).

$$\emptyset_{out}^2 = \left(\frac{K_{pd}F(s)K_0}{s + K_{pd}F(s)K_0}\right)^2$$
$$\frac{\left(\frac{1}{R_m}\right)^2 ({v_{nr}}^2 + {v_{ndrv}}^2 + {v_{ndac}}^2) + \left(\frac{2Q\Delta\omega}{Z_{pre}}\right)^2 ({v_{npre}}^2 + {v_{nadc}}^2)}{{i_r}^2(1 + 2Q\Delta\omega)^2} \tag{4.25}$$

Thus, the phase noise is band limited by use of PLL as in Equation 4.25. When the closed loop bandwidth of the PLL is increased the phase noise at the higher frequencies enters the loop and the integrated noise increases.

CHAPTER 5

DIGITAL CONTROL SYSTEM IMPLEMENTATION AND TEST RESULTS

The FM gyroscope takes a direct reading of the angular rate as a frequency and converts it to a digital signal by measuring it against a precise clock. The design of a FM gyroscope is primarily dependent on frequency reading performance, whereas amplitude is the most critical characteristic in an AM gyroscope.

This chapter discusses the general structure of FM gyroscope, PLL design criterias, performance and noise calculations, and results.

5.1 General Structure

The FM gyroscope's functioning and computations have been covered in earlier chapters. The digitally implemented FM gyroscope will be explored in this chapter. This design employs a quad-mass non-symmetric tuning fork type MEMS gyroscope as a transducer. This transducer's two channels oscillated as a coupled oscillator with mismatched amplitude and defined frequency mismatch (Δf).

The operation of the digitally controlled FM gyroscope includes two oscillator sustaining loops and other computation units realized with a 32-bit ARM M4 based digital microcontroller. Its operation starts with the conversion of the tiny currents generated by the motion of the resonators to the voltage. This conversion is done by using transimpedance type pre-amplifiers.

After getting the voltage value, this signal is converted and acquired by the microcontroller by using a 16 bits SAR ADC operated at 240kSPS. To start the oscillation, standard automatic gain controller(AGC) structure is operated similar with analog counterpart. After reaching some level of oscillation, digital PLL starts its operation to lock the phase and frequency of the incoming signal. After locking

the frequency, automatic gain controller is stopped, and the operation of the PLL and automatic amplitude controller(AAC) are started to control the frequency and the oscillation amplitude simultaneously.

The signals generated by the digitally controlled oscillator of the PLL and the output of the AAC are multiplied to excite the resonator. The excitation signal is generated by using a 16 bits 8-channel DAC controlled by the microcontroller. This DAC is operated at 80kHz refresh rate.

LFM control and computations are carried out after getting the sustained oscillations in the coupled oscillators of the FM gyroscope.

The frequency split is controlled by frequency split controller, befor the computation of LFM. This is accomplished by reading the frequency data from the PLL and adjusting the second resonator's proof mass voltage. A DAC is also used to adjust the proof mass voltage.

To obtain the rate information, the LFM computations are initiated after setting the frequency split to 20Hz. The sum of the frequencies is demodulated using the sine of the phase difference. The details will be discussed the preceding section to determine rate.

The block diagram of the implemented digital FM gyroscope can be seen at Figure 5.1, including:

- MEMS Structure,
- Preamplifiers,
- ADCs and DACs
- Start-up Controller
- Automatic Gain Controller (AGC)
- Phase Locked Loop (PLL)
- Automatic Amplitude Controller (AAC)
- Frequency Split Controller (FSC)
- Quadrature Controller (QC)

- Trigonometric Function Generator (TFG)
- Lissajous FM Computation Unit (LCU)

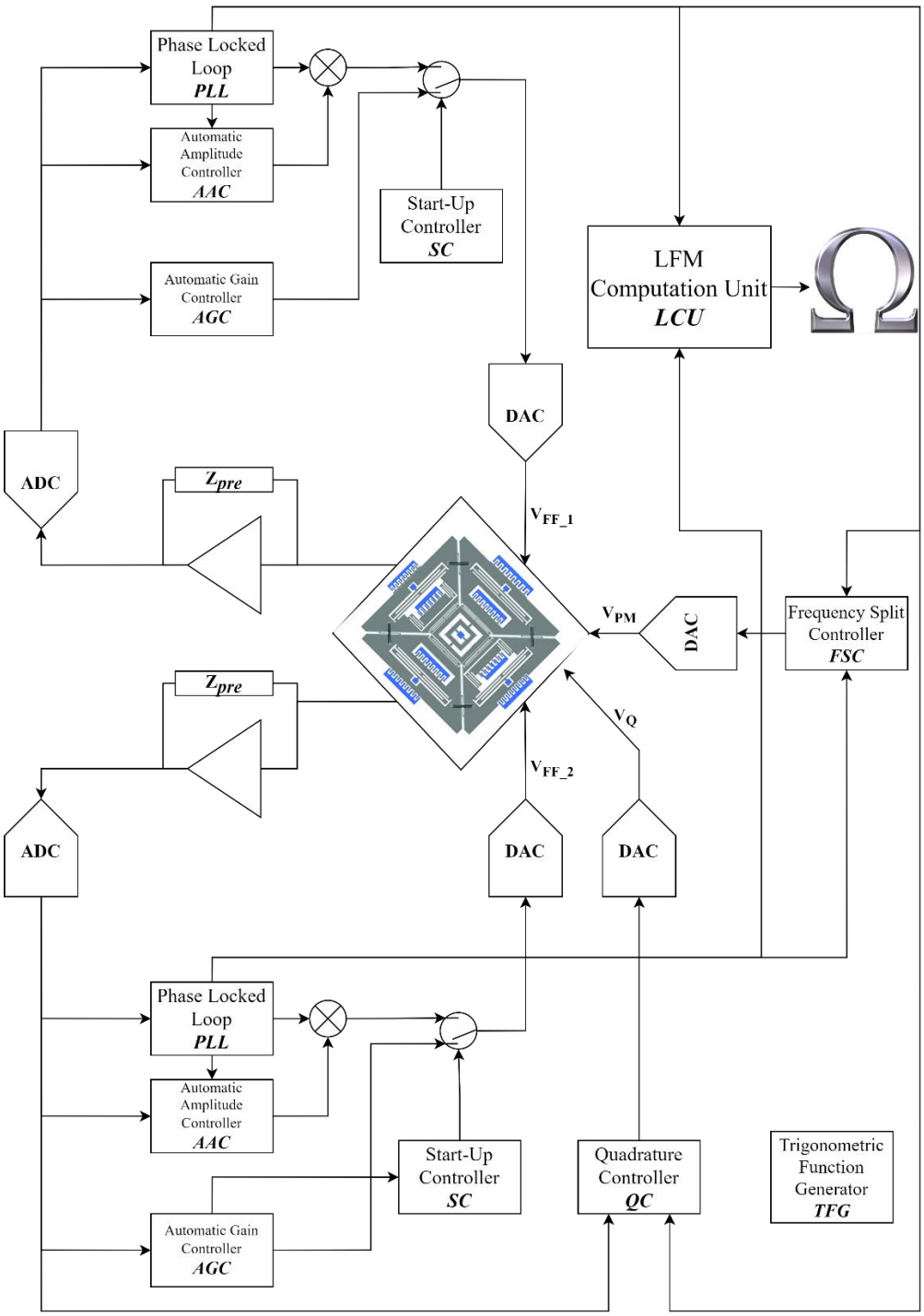

Figure 5.1. The block diagram of the digitally controlled FM gyroscope.

The Phase Locked Loop (PLL) is the most important component of this FM gyroscope because the output is frequency, and the frequency control and stability define the gyroscope's performance.

The following part will go over the specifics of the PLL design and performance measurements. Furthermore, the LFM and noise performance calculations will be performed.

5.2 PLL Design

A Phase-locked loop is a system that allows one system to follow another. It synchronizes the phase and frequency of an output signal with a reference. Instead of seeing the two signals as functions of time, consider them as phasors on the complex plane. As complex phasors, the two signals are two vectors that revolve around the plane. In general, the phase at any given moment is dependent upon time.

$$\theta_n(t) = \int_{-\infty}^{t} \omega_n(t)dt \tag{5.1}$$

The phase is the main point of the PLL design. Consider the situation when the first vector rotates at a constant angular frequency, $\omega_1(t) = \omega_c$. The second signal must modify its phase to reduce the distance from the reference, or the phase error, represented by the symbol θ_e, in order to follow the input signal. Its angular frequency may be increased or decreased to change its phase. We say that two vectors are locked to one another when they are travelling at the same speed. Depending on the system architecture, the phase error between the two systems is either zero or constant in the locked state. A control system intervenes on the second system to reduce the phase error if the reference signal differs from its present angular frequency.

Phase locked loops are mostly used in two areas. The PLL is required to demodulate the received signal back to baseband when analog signals are modulating a high-

frequency carrier. The second use is in frequency synthesis, which is the process of producing signals with accurate and steady frequencies.

5.2.1 Building Block of the PLL

Linear PLLs is the first class of PLLs. Digital PLLs and All Digital PLLs are two additional PLL types. The software PLL (SPLL), which is the last class, is operating on a processor that is under the control of an appropriate program.

To begin with, the linear PLL will be modeled in order to develop the PLL's theory. As shown in Figure 5.2, linear PLLs primarily consist of three components. It is necessary to first compare the phases of the reference input and the generated signal in some way. One method of doing that is to perform a straightforward multiplication followed by a filtering operation by the loop filter, which is the second part of the linear PLL. A voltage-controlled oscillator(VCO) is then fed with the filtered phase signal.

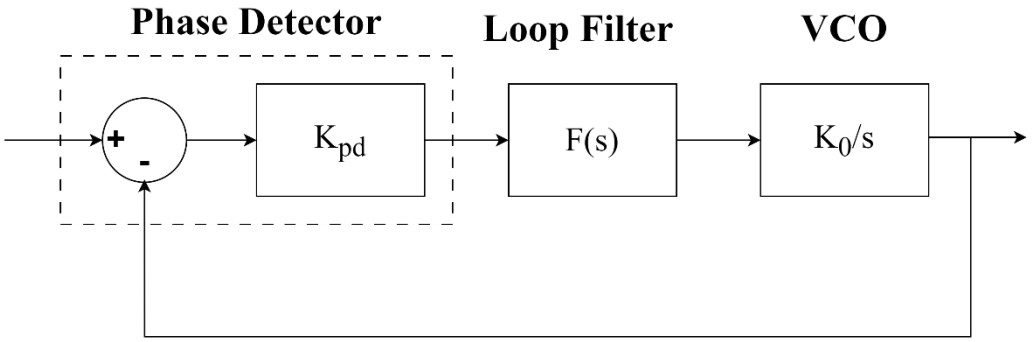

Figure 5.2. Block diagram of a linear PLL.

The Linear PLL is not as linear as one might assume given its name. However, as a first approximation, a linear model can be created.

5.2.2 PLL Linearization

Given that the PLL's input and output are phase signals, we can analyze the system using the transfer function H(s). As a result, we view the system as linear in terms of phase relationships. Additionally, we consider the linear PLL to be locked. The transfer function is defined by the Laplace transforms of the input and output phase functions, θin(t) and θout(t), respectively.

$$H(s) = \frac{\emptyset_{out}(s)}{\emptyset_{in}(s)} \tag{5.2}$$

The function H(s) is now a phase transfer function, and the model only works when the phase of the reference signal changes by very small amounts; if the phase error is too great, the Linear PLL will unlock and a nonlinear process will occur. Despite the fact that this process is characterized by a nonlinear differential equation.

We need to understand the transfer functions of the three Linear PLL building components, as shown in Figure 5.2, in order to express H(s). Since a PLL is nothing more than a control system for phase signals, we may use fundamental control theory to describe the linear model.

5.2.3 Phase Detector Linearization

The input to the phase detector is sine wave in FM gyroscope,

$$u_{in}(t) = U_{in} \sin(\omega_{in} t + \theta_{in}) \tag{5.3}$$

The VCO signal is also sinusoidal wave with cos function to make the linearization easier,

$$u_{fb}(t) = U_{fb}\cos(\omega_{fb}t + \theta_{fb}) \tag{5.4}$$

The phase difference between two signals is calculated by multiplying them and then filtering the output. That is the phase detector's primary function. The behavior must be represented in a linear form. Assuming the PLL is near or locked in frequency, we have $\omega = \omega_{in} = \omega_{fb}$ and the operation becomes

$$u_d(t) = U_{in}\sin(\omega_{in}t + \theta_{in})\, U_{fb}\cos(\omega_{fb}t + \theta_{fb}) \tag{5.5}$$

The equation above can be simplified by using the trigonometric relation below

$$\sin(\alpha)\cos(\beta) = \frac{1}{2}(\sin(\alpha + \beta) + \sin(\alpha - \beta)) \tag{5.6}$$

The phase detector's output is as follows:

$$u_d(t) = \frac{U_{in}U_{fb}}{2}\left(\sin(\theta_{in} + \theta_{fb} + 2\omega t) + \sin(\theta_{in} - \theta_{fb})\right) \tag{5.7}$$

The phase detector output has DC and high frequency components. High frequency components will be filtered out by the next stage, because of that the simplified input/output relationship of the phase detector becomes

$$u_d(t) = K_d\sin(\theta_e) \tag{5.8}$$

Sinusoidal signals can be linearized when the phase error is small

$$u_d(t) \approx K_d \theta_e \tag{5.9}$$

Thus, the linearized model is just a zero-order block having gain $K_d = \frac{U_{in}U_{fb}}{2}$.

5.2.4 Voltage Controlled Oscillator

The VCO produces a sinusoidal signal whose frequency is proportional to the input signal level. It operates at a quiescent frequency ω_c, preferably in close proximity to the signal we wish to lock on. VCO output is denoted by the VCO gain parameter K_0, the quiescent frequency ω_c, and the VCO control input u_f.

$$u_{out}(t) = \cos\left(\omega_c t + K_0 u_f(t)\right) \tag{5.10}$$

It can be freely chosen while creating the PLL in software because the filter design will support it.

The purpose of the linearized modeling is to get the phase transfer function of the system. Therefore, phase information should be obtained from the VCO by integration of the frequency variation $K_0 u_f(t)$.

$$\theta_{out}(t) = \int K_0 u_f(t) dt = K_0 \int u_f(t) dt \tag{5.11}$$

The integration's Laplace transform is 1/s. Consequently, the Laplace transform for the output phase θ_{out} is as follows:

$$\emptyset_{out}(s) = \frac{K_0}{s} U_f(s) \tag{5.12}$$

Thus, the VCO is like an integrator in the phase control loop.

5.2.5 Loop Filter

The loop filter is used for filtering the high frequency components of the phase detector output; but it can also be used to control the VCO to decrease the phase error. The PLL is a control system for phase signals, the loop filter is the regulator. The loop filter maintains the desired phase delay and also reject the disturbances coming outside of the control system. When determining how well a regulator can cope with the two tasks several properties can be studied. Properties such as stability, speed, and static accuracy.

- **Stability**

This is most likely the most critical, and thus most complicated, component of the PLL. The model developed in this chapter can be used to analyze the stability of linear systems. Once the filter type is selected, stability difficulties are described further below.

- **Static Accuracy:**

The PLL is linearized and maintained at zero phase error. Because of the non-linear properties of the PLL, stability may be lost if the system has more phase error than it can handle. As a result, for every sort of input change, the error should be

asymptotically zero. Whatever action is taken at the input must be handled by the regulator.

- **Speed:**

The speed of a control system is another significant characteristic. When the desired value is modified in any way, it takes some time for the system's output to change and eventually settle at the new value. The rising time is one of the most common speed measurements. The rise time is defined as the amount of time required for the output to increase from 10% to 90% of its final value. The bandwidth is another speed metrics that defines the highest frequency that the system can follow.

- **Filter Type**

The output signal $u_d(t)$ of the phase detector consists of a number of terms. In the locked state of the PLL, the first of these is a DC component that is roughly proportional to the phase error θ_e, the remaining terms are AC components.

These high frequency terms must be filtered out by the loop filter. The loop filter must pass the lower frequency signal and suppress the higher, because of that it must have low pass filter characteristics. Best [31] mentions three basic filter types common in PLL applications: the passive lead-lag filter, the active lead-lag filter, and the active PI filter. These filters can be used with a voltage output phase detector different from the charge pump type detectors.

- **Passive lead-lag filter**

First order passive lead-lag filter as in Figure 5.3 having one pole and one zero. The transfer function of this filter is as follow:

$$F(s) = \frac{U_f(s)}{U_d(s)} = \frac{1 + s\tau_2}{1 + s(\tau_2 + \tau_1)} \tag{5.13}$$

τ_1 and τ_2 can be defined as R_1C_1 and R_2C_1 respectively. The phase lead characteristics comes from zero in the numerator, whereas the pole in the denominator produces the phase lag.

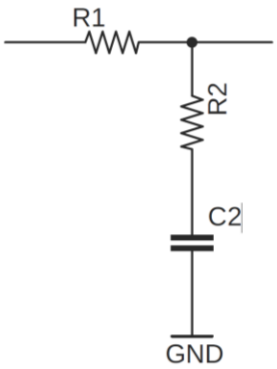

Figure 5.3. Passive lead-lag filter.

The amplitude and phase response of the passive lead-lag loop filter is shown in Figure 5.4.

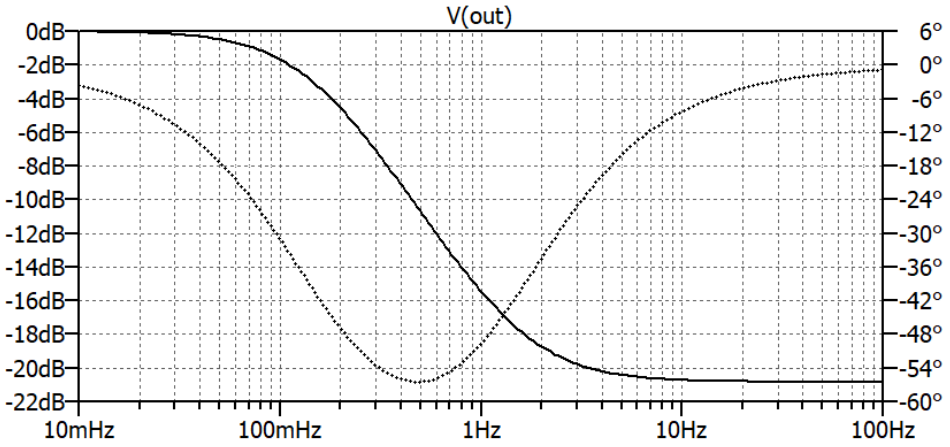

Figure 5.4. The amplitude and phase response of the passive lead-lag loop filter.

- **Active lead-lag filter**

First order passive lead-lag filter having one pole and one zero can be found at Figure 5.5. The transfer function of this filter is as follow:

$$F(s) = \frac{U_f(s)}{U_d(s)} = K_0 \frac{1+s\tau_2}{1+s\tau_1} \tag{5.14}$$

τ_1 and τ_2 can be defined as R_1C_1 and R_2C_1 respectively; but active lead-lag filter has also gain component as $K_0 = \frac{C_1}{C_2}$. The phase lead characteristics comes from zero in the numerator, whereas the pole in the denominator produces the phase lag.

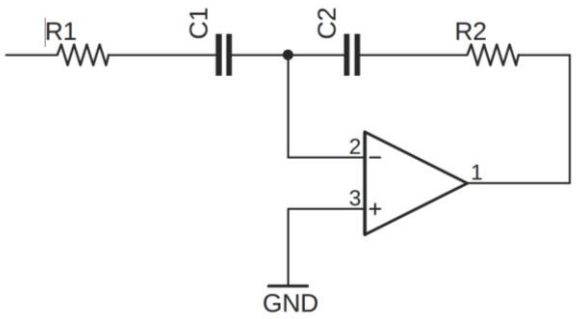

Figure 5.5. Active lead-lag filter.

The amplitude and phase response of the passive lead-lag loop filter is shown in Figure 5.6.

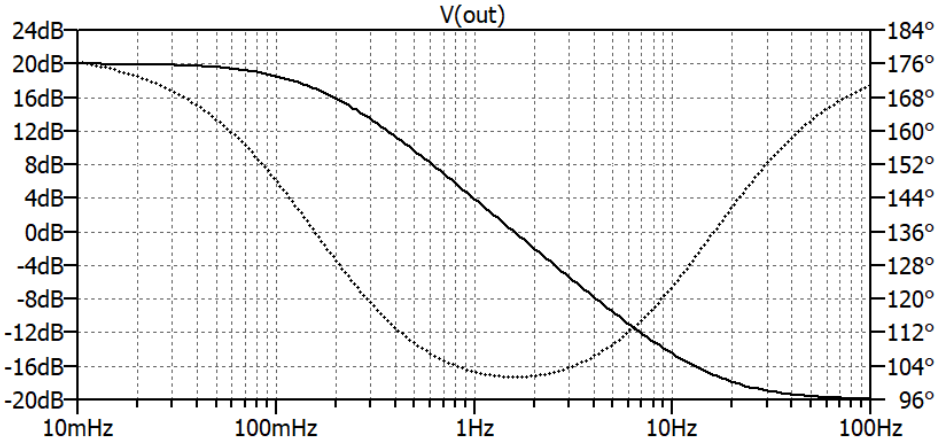

Figure 5.6. The amplitude and phase response of the active lead-lag loop filter.

- **Active PI filter**

This is another active loop filter having low pass filtering characteristics. PI filter can also be used in the instrumentation control as "proportional + integral" controller. The transfer function of the PI filter can be expressed below:

$$F(s) = \frac{U_f(s)}{U_d(s)} = \frac{1 + s\tau_2}{s\tau_1} \tag{5.15}$$

The PI filter has a pole at zero like in an integrator, because of that, it has infinite gain at DC to eliminate steady state errors.

The circuit diagram and its bode plot can be seen at Figure 5.7 and Figure 5.8 respectively.

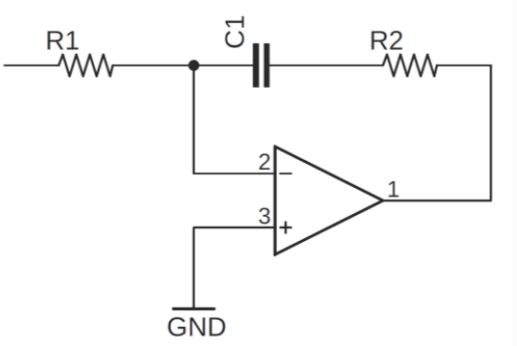

Figure 5.7. Active PI filter.

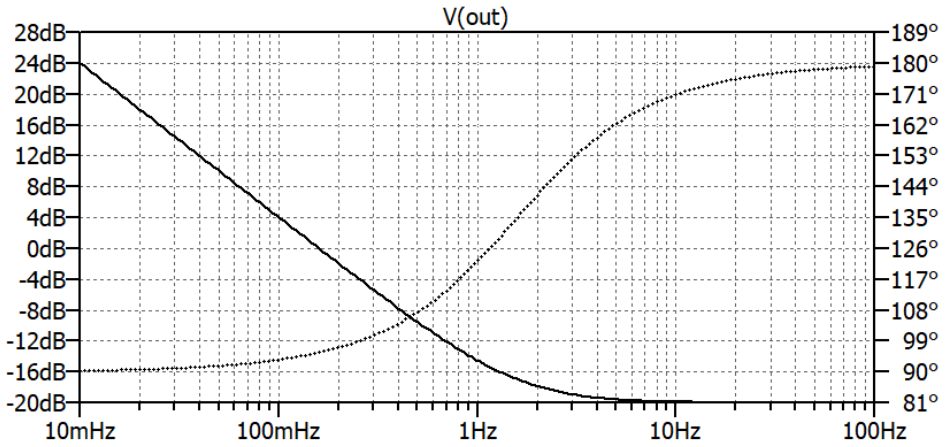

Figure 5.8. The amplitude and phase response of the active PI loop filter.

- **Higher order loop filters**

Reference frequency feedthrough has an impact on the spectral purity of PLL frequency synthesizers. If the loop filter does not sufficiently attenuate the AC components at the reference frequency that are generated by the phase detector, spurious sidebands may be intolerable. To limit reference frequency feedthrough, higher-order loop filters are required.

With higher-order loop filters, loop stability becomes an issue. Getting stable operation with a second-order PLL was easy because the open-loop transfer function had two poles and one zero. A pole creates a phase shift of −90° at higher frequencies, and a zero creates a phase shift of +90°. When the poles and the zero are properly located, the overall phase shift never comes close to −180°; hence, the loop stays stable. This goal was easily met by choosing time constant τ_2 of the loop filter such that a reasonable damping factor ζ was obtained. If the loop filter has two or more poles, the phase shift can become larger than 180°, hence the poles and zeroes of the loop filter must be placed such that stability is maintained.

Higher order loop filters can be obtained by adding a second order lowpass filter to the loop filter as in Figure 5.9.

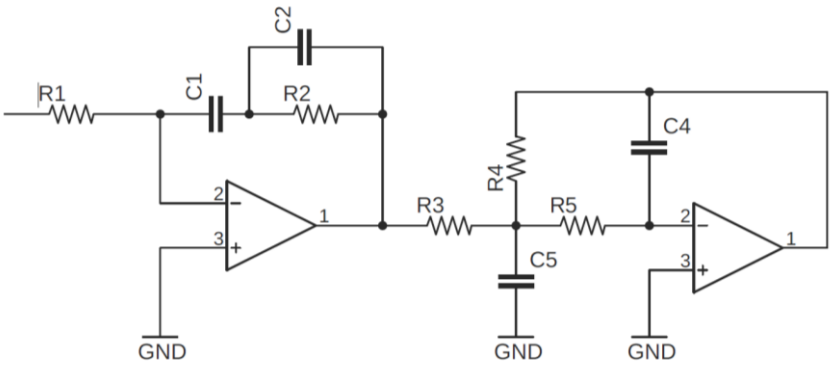

Figure 5.9. Fourth order active PI loop filter.

This filter has a second-order PI filter and a two-pole low-pass filter. The transfer function of this filter as follow:

$$F(s) = \frac{U_f(s)}{U_d(s)} = \frac{1 + s(\tau_2 + \tau_3)}{s\tau_1(1 + s\,\tau_3)} \frac{1}{(1 + s\tau_4)\,(1 + s\tau_5)} \tag{5.16}$$

The poles of the PI are located at $s = 0$, $s = \omega_3$ and the zero of the PI is located at $s = \omega_2$. The second order low-pass filter can have real poles or complex-conjugate pole pair. However, generally low-pass filter with complex-conjugate pole pair is used. The transfer function for this case can be expressed as

$$F(s) = \frac{U_f(s)}{U_d(s)} = \frac{1 + s(\tau_2 + \tau_3)}{s\tau_1(1 + s\,\tau_3)} \frac{1}{1 + \frac{2s\zeta}{\omega_s} + \frac{s^2}{\omega_s^2}_T} \tag{5.17}$$

5.2.6 PLL Control Loop Design

There are so many methods in the control theory to analyze the stability of feedback system. We will use the bode plot method to analyze and design the control loop of the PLL.

To analyze stability, the bode diagram is plotted by importing $j\omega$ in s in the open loop transfer function. The magnitude curve crosses the 0-dB line at a radian frequency named transition frequency ω_T. At the transition frequency, the open-loop gain is exactly 1. The system is stable if the phase of G(ω_T) is more positive than −180°. In this frequency, phase margin is described as $\emptyset_m = 180 + \emptyset(\omega_T)$. Phase margin is generaly be designed in range between 30 and 60 degrees. In our design this value will be 45 by coinsiding the zero of the filters with transition frequency ω_T.

In the design, we wanted to obtain maximum roll off slope to suppress the high frequency component; because of that the only one zero is inserted in the loop and 5 poles are inserted. However, poles create stability problems. To solve the stability problems, poles are located away from the transition frequency.

The poles and the zero of the system are placed with reference to the transition frequency ω_T. Consequently, the loop design can start with an initial value for ω_T. According to the desired PLL loop bandwidth, ω_T is determined. For a 3-dB closed loop bandwidth with damping ratio of 0.7, ω_T can be expressed as

$$\omega_T \approx \frac{\omega_{3dB}}{1.33} \tag{5.18}$$

This ratio stays nearly unchanged for higher-order PLL. This is a consequence of the fact that we always try to shape the magnitude plot such that its magnitude curve crosses the 0-dB line with a slope of about −20 dB/decade.

5.2.7 Controller Design for The First and Second Resonant Modes

PLL design for the resonator is done in the analog domain, and then the digital counterpart is designed in software. The center frequency of the resonators in FM gyroscope is 10kHz and desired PLL bandwidth is 100Hz for both of the modes. Because of that the PLL design is same for the modes, the only difference is the oscillation amplitude determined by the automatic amplitude controller.

PLL is designed with a model shown in Figure 5.10. The loop filter inside the loop is chosen as 4th order active PI controller as in Figure 5.9. The reason for this controller is to filter the high frequency components resulting from the phase detector and to decrease the phase error to zero with infinite gain at DC.

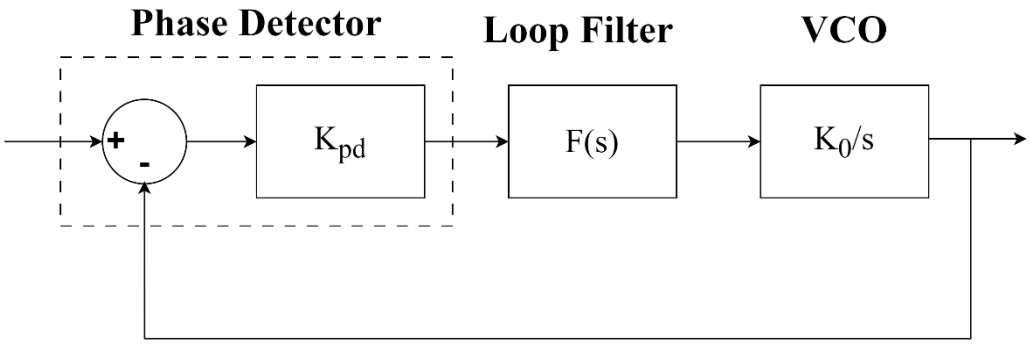

Figure 5.10. Linearized PLL block diagram.

The controller design starts with writing the open loop transfer function of the system. Our PLL system has 3 components, phase detector, loop filter, and VCO. The transfer functions of them are derived at previous sections. Now, we can write the open loop transfer function as in Equation below.

$$G(s) = K_{pd}F(s)\frac{K_0}{s} = \frac{K_0K_d}{s}\,\frac{1+s(T_2)}{sT_1(1+s\,T_3)}\,\frac{1}{1+\frac{2s\zeta}{\omega_s}+\frac{s^2}{\omega_s^2}_T} \qquad (5.19)$$

Where $T_1 = \tau_1$, $T_2 = \tau_2 + \tau_3 = \frac{1}{\omega_2}$, and $T_3 = \tau_3 = \frac{1}{\omega_3}$.

The loop filter has poles at $s = 0$ and $s = \omega_3$, and a zero at $s = \omega_2$. The poles of the 2-pole filter are located as complex-conjugate at ω_s. With these poles and zero, at low frequency, we have -40 dB/decade. When we reach zero at ω_2, the slope becomes -20 dB/decade. If we place the ω_3, after the ω_2, slope becomes -40 dB/decade again. To further decrease the high frequency noises, we can place the ω_s after the ω_3. The last placement of ω_s provides -80 dB/decade at high frequencies.

After deciding the pole and zero placement order, we can define a procedure for the placement of them.

At first, the desired bandwidth of the PLL system should be decided. In our case, ω_{3dB} bandwidth will be 100Hz; but it is generally be chosen as $\frac{\omega_0}{20}$ or lower. Then, we can calculate the transition frequency in Equation 5.20 as stated in Equation 5.18. The gain at ω_2 is set 1.

$$\omega_2 = \frac{K_0 K_d}{{\omega_T}^2} = \omega_T \approx \frac{\omega_{3dB}}{1.33} = 75Hz = 471 \text{ rad/sec} \tag{5.20}$$

After that we can decide the ω_3. When we add ω_3 near to the ω_2, high frequency filtering effect improves; but the decrease in the phase margin leads stability problems. The appropriate placement of ω_3 is the 5 times the ω_2 in the loop as.

$$\omega_3 = 5\omega_2 = 75 * 5 = 375Hz = 2355 \text{ rad/sec} \tag{5.21}$$

To make the ω_2 is the transition frequency, T_1 should be chosen that provides the open-loop gain is 1 at ω_2. T_1 can be expressed below:

$$T_1 = \frac{K_0 K_d}{{\omega_T}^2} = \frac{1 * 0.5}{222} = 2.25e - 6 \tag{5.22}$$

Thus we should chose the appropriate values for ω_s and ζ of the 2-pole low pass filter. Generally, the damping factor is chosen as 0.7 for this type of filter, and ζ is chosen as 0.7. Then, the poles of this filter should be placed where it does not deteriorate the phase margin of the system. The sufficient margin can be obtained by applying the rule below

$$\omega_s = 5\,\omega_3 = \ 5 * 2355 = 11775\,rad/sec \tag{5.23}$$

Finally, we have obtained the open loop transfer function as in Figure 5.11.

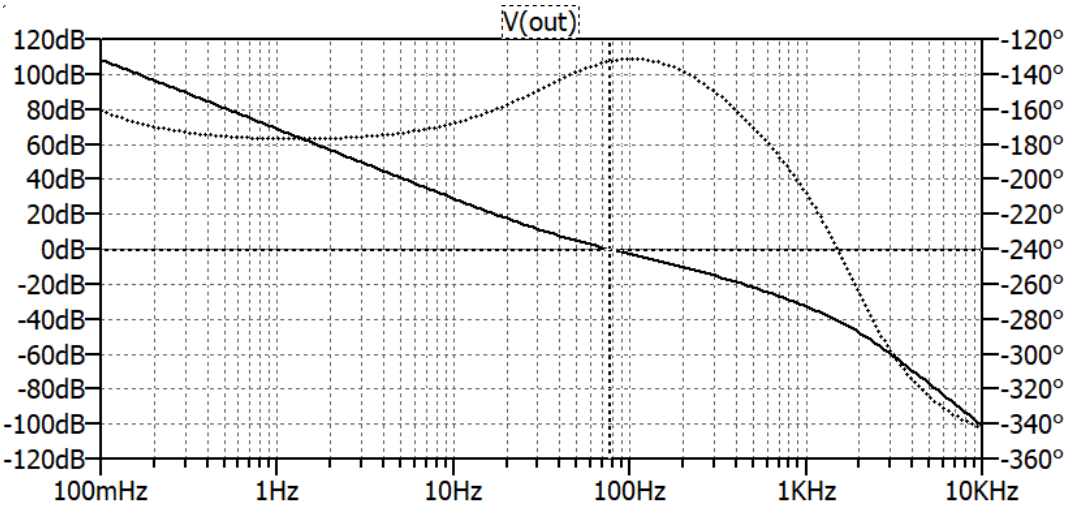

Figure 5.11. The open loop transfer function of the designed PLL control loop. Phase margin: 47°, Gain Margin: 25dB.

When we analyze the closed loop transfer function, we can obtain the 3dB and -90° phase shift bandwidth of the PLL. Figure 5.12 shows the closed loop transfer function. .

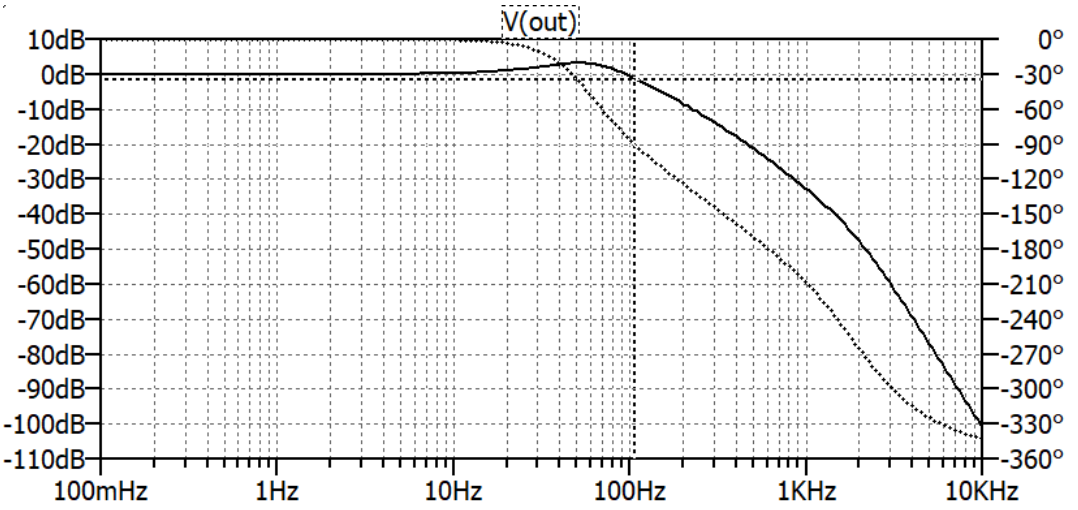

Figure 5.12. The closed loop transfer function of the designed PLL control loop. 90° phase shift bandwidth: 104Hz, -3dB bandwidth: 125Hz.

After we obtain the closed loop transfer function, the step response of the closed loop PLL system is simulated as shown in Figure 5.13. The system settles in 30ms.

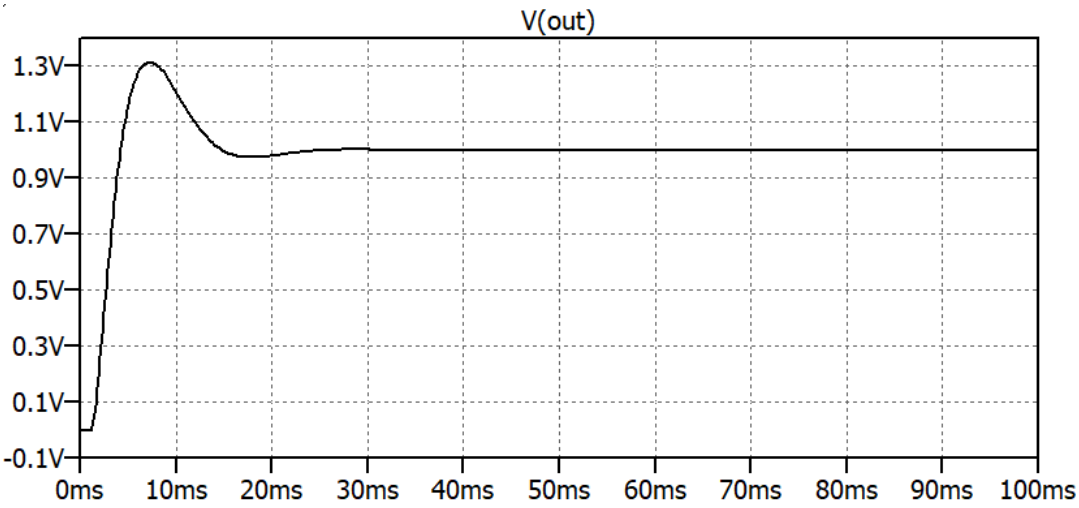

Figure 5.13. The step response of the closed loop PLL system. Settling time: 30msec.

5.3 LFM Operation

At first, the two oscillation modes are oscillated and locked with a digital PLL inside the loop. The PLLs inside the two oscillating loops provide the direct frequency reading from the oscillators. After we obtain the oscillation frequencies, frequency split is adjusted by tuning the prof mass of the second mode to predefined frequency.

The operation of the LFM gyroscope relies on modulating the rate sensitivity at the frequency split of the modes.

The instantaneous frequencies of the two modes can be expressed below:

$$\dot{\emptyset}_x = \omega_{ox} - \alpha_z \frac{V_y}{V_x} \Omega_z \sin \Delta\emptyset_{xy} \tag{5.24}$$

$$\dot{\emptyset}_y = \omega_{oy} - \alpha_z \frac{V_x}{V_y} \Omega_z \sin \Delta\emptyset_{xy} \tag{5.25}$$

The frequency sum gives the rate dependent out as in Equation below. However, this equation has very high DC component coming from the mechanical resonant frequencies.

$$\sum \dot{\emptyset}_{xy} = \omega_{ox} + \omega_{oy} - \left(\frac{V_y}{V_x} + \frac{V_x}{V_y}\right) \alpha_z \Omega_z \sin \Delta\emptyset_{xy} \tag{5.26}$$

In order to suppress the DC component of the sum of frequencies, very low cut-off frequency high pass filter is used. After filtering the signal, we have rate signal modulated by the phase difference between the modes.

Rate information can be obtained from this signal by modulating with sine of the phase difference. In an analog PLL driven systems, the acquisition of the phase is diffucult to obtain; but in the digital PLL, we can acquire the phase difference from the software. After doing the modulation we have obtained the signal below:

$$\sin \Delta\emptyset_{xy}\, h_{HPF} \sum \dot{\emptyset}_{xy} \approx -\frac{1}{2}\left(\frac{V_y}{V_x}+\frac{V_x}{V_y}\right)\alpha_z \Omega_z\left(1-\cos 2\Delta\emptyset_{xy}\right) \qquad (5.27)$$

Now, we have obtained the rate signal with DC and $\cos 2\Delta\emptyset_{xy}$ components. The image at $2\Delta\emptyset_{xy}$ can be suppressed by using a low pass filter at the output of the modulator. Finally, we get the rate out from the frequency outputs as follow:

$$h_{LPF}\left(\sin \Delta\emptyset_{xy}\, h_{HPF} \sum \dot{\emptyset}_{xy}\right) \approx -\frac{1}{2}\left(\frac{V_y}{V_x}+\frac{V_x}{V_y}\right)\alpha_z \Omega_z \qquad (5.28)$$

Thus, in this equation, phase is the directly related with the velocity ratios and the angular gain. Therefore, we obtained a very short definition of the rate that has very low mechanical and electrical sensor parameters.

5.4 Noise Performance of LFM Gyroscope

In this part, the mechanical and electrical parameters of the digitally controlled FM gyroscope will be used to figure out the phase noise of the first and second modes with digital PLL inside the loop.

The mechanical parameters of the MEMS gyroscope sensor chip can be seen at Table 5.1. The gyroscope has a non-symmetric structure for the first and second modes. Therefore, the noise calculations for these modes will be calculated separately as follow.

Table 5.1 Mechanical parameters of the MEMS gyroscope sensor chip.

Parameters	First mode	Second mode
Resonant frequency (Hz)	7636	7656
Capacitive gap (μm)	2.6	2.6
Capacitance (fF)	776	5160
Mass (kg)	5.15E-08	6.15E-08
Proof mass voltage (V)	26.3	26.3
Quality factor	100,000	10,000

5.4.1 Noise Calculations for The First Mode:

The first mode is oscillated with 5μm displacement, and operated at 7636 Hz with 20Hz frequency-split with second mode. The system model used in the Chapter 4 for the oscillator with digital PLL will be used in this calculation.

The modeling parameters and the details of the noise derivations can be found at Chapter 4.

At first, the impedance of the oscillator should be defined as follow

$$Z_L = 2j\omega L_m \frac{(\omega_n - \omega_s)}{\omega} = 2j\omega Q R_m \frac{(\Delta\omega)}{\omega} \tag{5.29}$$

For the first mode of the FM gyroscope, $R_m = 100k\Omega$ and $Q = 100000$.

After that, we should calculate the noises at the nodes, v_{nr}, v_{ndrv}, v_{ndac}, v_{npre}, and v_{nadc}.

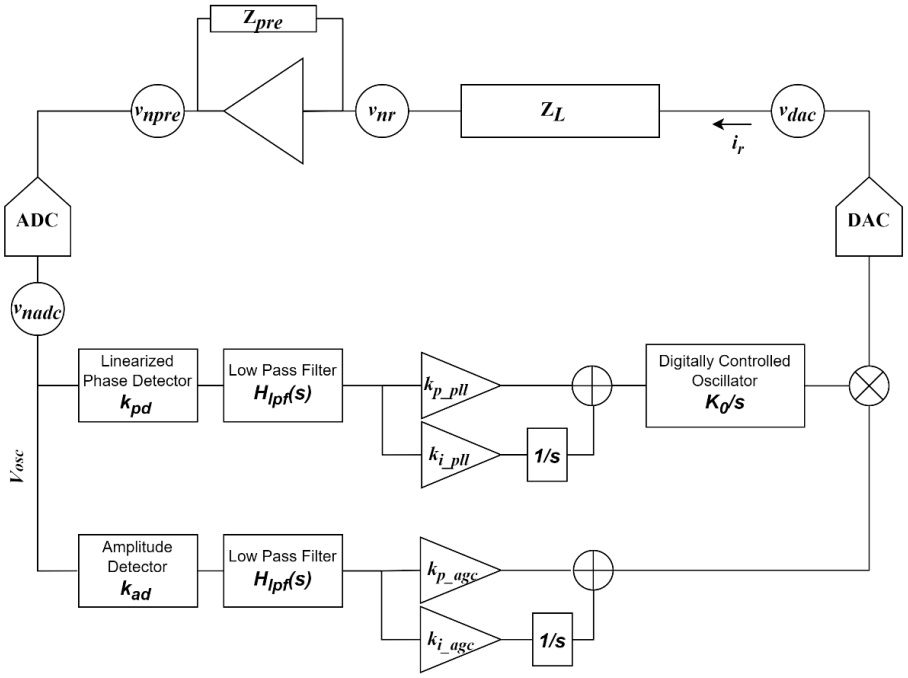

Figure 5.14.The simplified circuit model of the oscillator with digital PLL.

The mechanical noise of the oscillator v_{nr} can be calculated as

$$v_{nr} = \sqrt{4kTR_m} = 40nV/\sqrt{Hz} \tag{5.30}$$

The output of the DAC is directly fed to the resonator with a passive filter having very low noise compared with DAC noise, because of that v_{ndrv} is assumed zero. The noise at the DAC output can be calculated by using the refresh rate and SNR values of the DAC. However, DAC has also some constant noise limited by output buffer. The output noise of the DAC used in the system is 75nV/$\sqrt{Hz}$

$$v_{ndac} = 75nV/\sqrt{Hz} \tag{5.31}$$

The noise of the preamplifier can be calculated by the noise of the opamp and the passive components of the preamplifier. In this circuit, preamplifier is designed as resistive preamplifier. The preamplifier is also having some gain stage at the output; but during calculation, gain stage will be combined with preamplifier. The parameters of the preamplifier are below:

$$v_{npre} = 784nV/\sqrt{Hz} \tag{5.32}$$

$$Z_{pre} = 3M\Omega \tag{5.33}$$

The noise of the ADC input can be calculated by using the sampling rate and SNR values of the ADC. The sampling rate of the ADC is 240kSPS and the SNR of the ADC is 86dB. The noise of the ADC with these parameters and the 2.5V full scale input is as follow.

$$v_{nadc} = \frac{\frac{2.5}{2 * \sqrt{2}}}{10^{\frac{SNR}{20}}\sqrt{120000}} = 129nV/\sqrt{Hz} \tag{5.34}$$

Thus, the phase noise can be calculated by using the equation below by inserting the noise sources.

$$\emptyset_{out}^2 = \left(\frac{K_{pd}F(s)K_0}{s + K_{pd}F(s)K_0}\right)^2 \frac{\left(\frac{1}{R_m}\right)^2 ({v_{nr}}^2 + {v_{ndrv}}^2 + {v_{ndac}}^2) + \left(\frac{2Q\Delta\omega}{Z_{pre}}\right)^2 ({v_{npre}}^2 + {v_{nadc}}^2)}{{i_r}^2(1 + 2Q\Delta\omega)^2} \tag{5.35}$$

The transfer function coming from the PLL can be seen as a low pass filter for the phase noise, and the bandwidth of the PLL generally does not affect the spectral noise; but limits the integrated noise by filtering the phase noise.

The final result is written below with the only variable is $\Delta\omega$ and the graph can be seen at Figure 5.15.

$$\emptyset_{out}^2 = (H_{LPF}(s))^2 \frac{\left(\frac{1}{R_m}\right)^2 ({v_{nr}}^2 + {v_{ndrv}}^2 + {v_{ndac}}^2) + \left(\frac{2Q\Delta\omega}{Z_{pre}}\right)^2 ({v_{npre}}^2 + {v_{nadc}}^2)}{{i_r}^2(1 + 2Q\Delta\omega)^2} \quad (5.36)$$

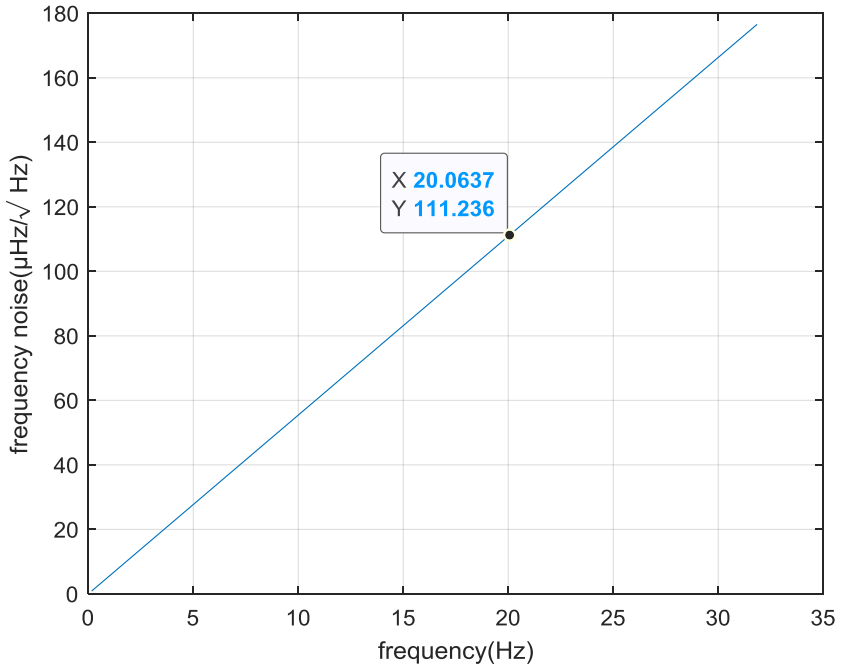

Figure 5.15. Frequency noise result of the first mode of the FM gyroscope. 111μHz/√Hz at 20Hz frequency split.

5.4.2 Noise Calculations for The Second Mode

The second mode is oscillated with 2nm displacement, and operated at 7656 Hz with 20Hz frequency-split with first mode. The system model in the Chapter 4 for the oscillator with digital PLL will be used in this calculation.

The modeling parameters and the details of the noise derivations can be found at Chapter 4.

At first, the impedance of the oscillator should be defined as follow

$$Z_L = 2j\omega L_m \frac{(\omega_n - \omega_s)}{\omega} = 2j\omega Q R_m \frac{(\Delta\omega)}{\omega} \tag{5.37}$$

For the second mode of the FM gyroscope, $R_m = 10M\Omega$ and $Q = 10000$.

After that, we should calculate the noises at the nodes, v_{nr}, v_{ndrv}, v_{ndac}, v_{npre}, and v_{nadc}.

The mechanical noise of the oscillator v_{nr} can be calculated as

$$v_{nr} = \sqrt{4kTR_m} = 400nV/\sqrt{Hz} \tag{5.38}$$

The output of the DAC is directly fed to the resonator with a passive filter having very low noise compared with DAC noise, because of that v_{ndrv} is assumed zero. The noise at the DAC output is same with the DAC noise of the first mode. The output noise of the DAC used in the system is 75nV/$\sqrt{Hz}$

$$v_{ndac} = 75nV/\sqrt{Hz} \tag{5.39}$$

The noise of the preamplifier can be calculated by the noise of the opamp and the passive components of the preamplifier. In this circuit, preamplifier is designed as capacitive preamplifier. The preamplifier is also have some gain stage at the output; but during calculation, gain stage will be combined with preamplifier. The parameters of the preamplifier are below:

$$v_{npre} = 5322nV/\sqrt{Hz} \tag{5.40}$$

$$Z_{pre} = 240M\Omega \tag{5.41}$$

The noise of the ADC input can be calculated by using the sampling rate and SNR values of the ADC. The sampling rate of the ADC is 240kSPS and the SNR of the ADC is 86dB. The noise of the ADC with these parameters and the 2.5V full scale input is as follow.

$$v_{nadc} = \frac{\frac{2.5}{2*\sqrt{2}}}{10^{\frac{SNR}{20}}\sqrt{120000}} = 129nV/\sqrt{Hz} \tag{5.42}$$

Thus, the phase noise can be calculated by using the equation below by inserting the noise sources.

$$\emptyset_{out}^2 = \left(\frac{K_{pd}F(s)K_0}{s + K_{pd}F(s)K_0}\right)^2 \frac{\left(\frac{1}{R_m}\right)^2 ({v_{nr}}^2 + {v_{ndrv}}^2 + {v_{ndac}}^2) + \left(\frac{2Q\Delta\omega}{Z_{pre}}\right)^2 ({v_{npre}}^2 + {v_{nadc}}^2)}{{i_r}^2(1 + 2Q\Delta\omega)^2} \tag{5.43}$$

The final result is written below with the only variable is $\Delta\omega$ and the graph can be seen at Figure 5.16.

$$\emptyset_{out}^2 = (H_{LPF}(s))^2$$

$$\frac{\left(\frac{1}{10e6}\right)^2 (400n^2 + 75n^2) + \left(\frac{2 \cdot 1000 \cdot \Delta\omega}{240e6}\right)^2 (5322n^2 + 129n^2)}{5n^2(1 + 2 \cdot 1000 \cdot \Delta\omega)^2} \quad (5.44)$$

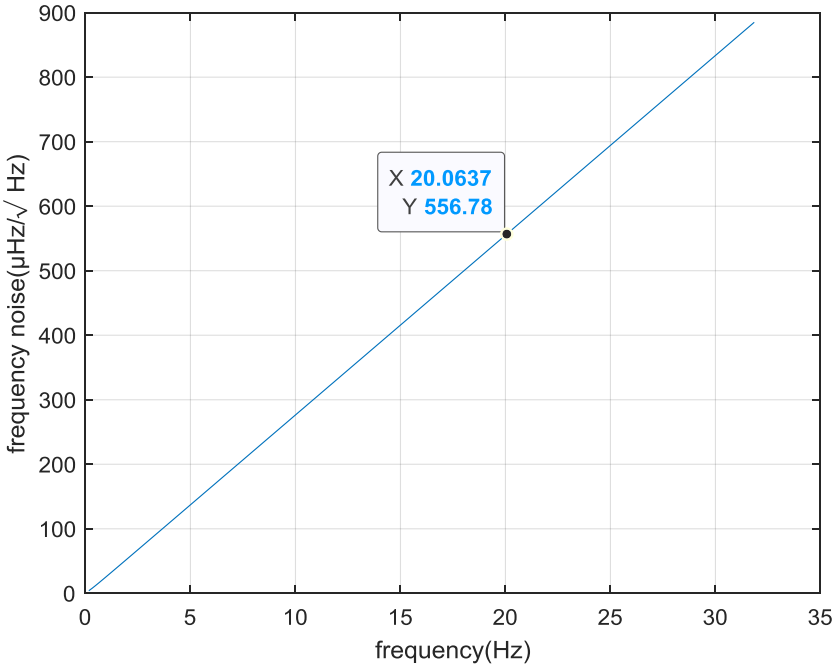

Figure 5.16. Frequency noise result of the second mode of the FM gyroscope. 556μHz/√Hz at 20Hz frequency split.

5.4.3 FM Gyroscope Rate Noise Calculation

In the FM gyroscope used in this thesis is operated as with 1:2500 amplitude mismatch to enhance the frequency reading capability by increasing the scale factor. In this operation frequency split is introduces as 20Hz between the modes to realize LFM operation. During the LFM operation the scale factor can be calculated as follow by using the Equation 5.28.

$$SF = -\frac{1}{2}\left(\frac{V_y}{V_x}+\frac{V_x}{V_y}\right)\alpha_z = -\frac{1}{2}\left(\frac{2n}{5u}+\frac{5u}{2n}\right)0.7 = 875\ \frac{Hz}{rad/sec} \qquad (5.45)$$

The rate noise can be calculated by using the scale factor and frequency noises calculated at previous section.

The frequency noises of the first and second mode at the 20Hz frequency split are 111μHz/√Hz and 556μHz/√Hz respectively. The total output noise can be calculated by combining the uncorrelated noises as follow

$$\begin{aligned} frequency\ output\ noise &= \sqrt{(111e(-6)^2 + 556e(-6)^2)} \\ &= 567\mu Hz/\sqrt{Hz} \end{aligned} \qquad (5.46)$$

$$\begin{aligned} rate\ output\ noise &= \frac{frequency\ output\ noise}{SF}180 * 3600 \\ &= 0.42°/hr/\sqrt{Hz} \end{aligned} \qquad (5.47)$$

The rate noise of the sensor is double sided and its noise characteristic is not white, because of that noise spectrum has higher noise at higher frequencies due to

quantization noise characteristics of the frequency reading. The noise spectrum can be seen at Figure 5.17.

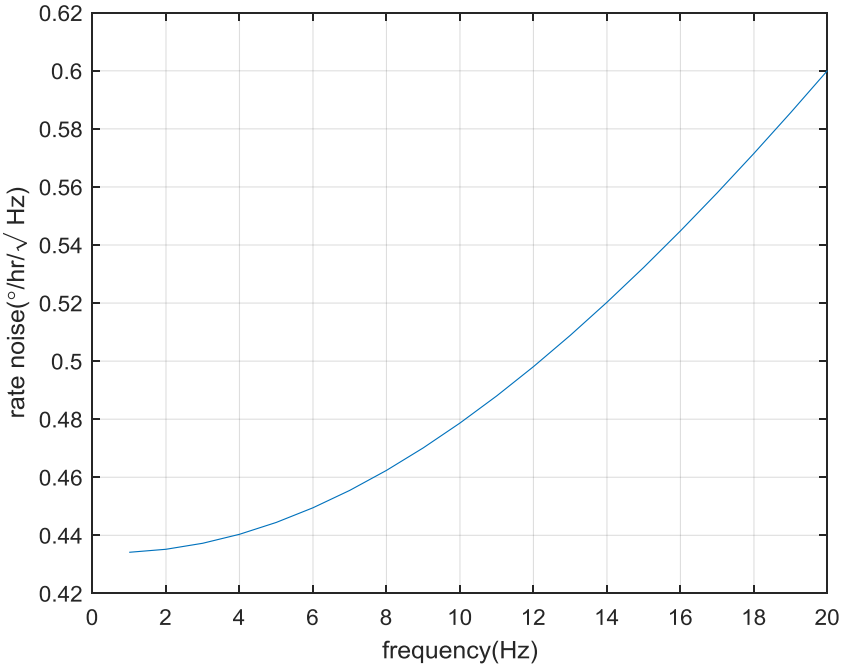

Figure 5.17. The rate noise spectrum of the FM Gyroscope.

The Allan Variance result can be obtained from the rate noise spectrum as in Figure 5.18

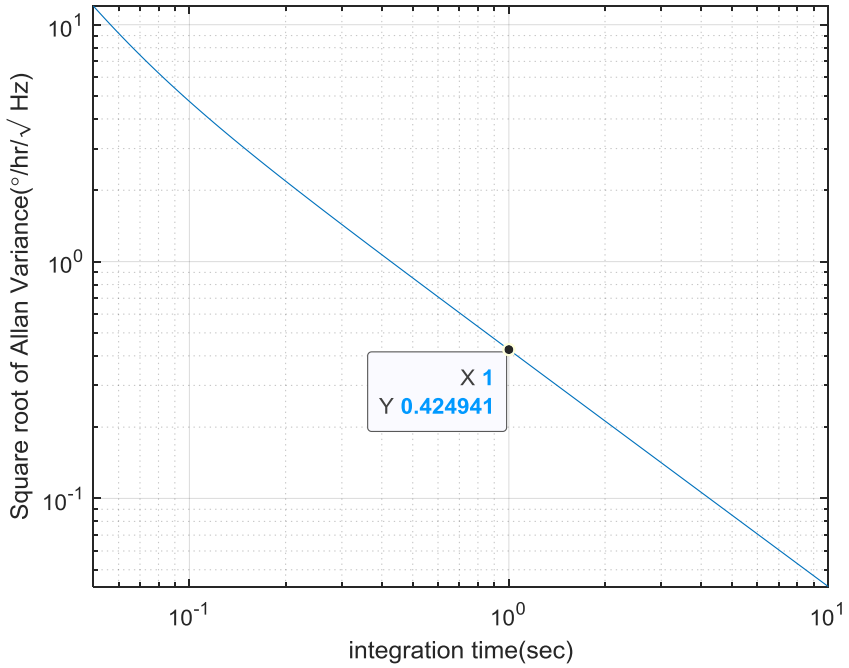

Figure 5.18. The Allan Variance analysis obtained from rate noise spectrum. ARW: 0.42°/hr/√Hz.

5.5 Test Results of the FM Gyroscope with Amplitude-Mismatch-Ratio

For testing, digitally controlled FM gyroscope circuit as in Figure 5.19 was connected to the non-symmetric quad-mass tuning fork gyroscope shown in Figure 5.20 with nominal $f_0 = 7.5kHz$. The quality factors of the first and second mode are $Q_1 = 100k$ and $Q_2 = 10k$ respectively. The resonators are oscillated inside the digital controller and acquired the frequencies at the same time by use of digital PLL. The output of the PLL is used to extract the rate information by doing some modulations and filtering related with LFM gyroscope.

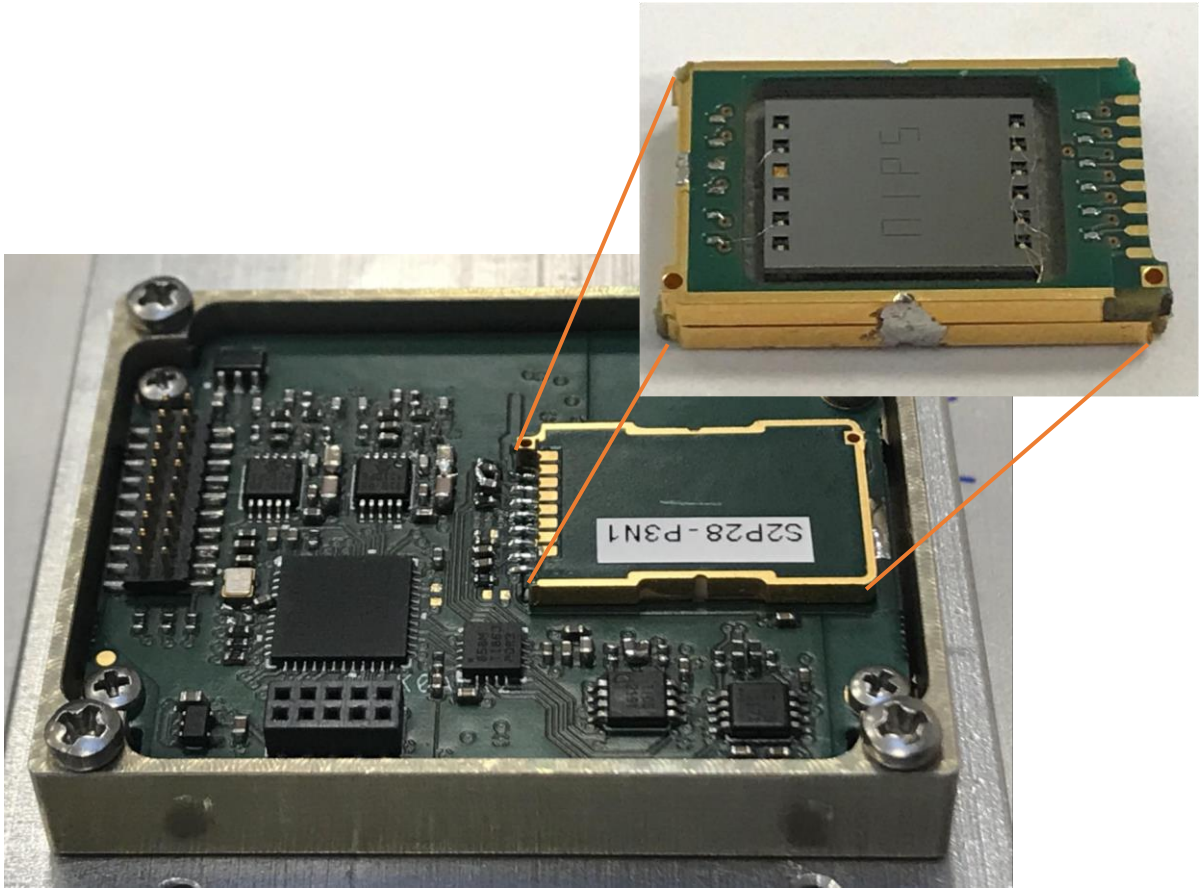

Figure 5.19. Digitally controlled FM gyroscope readout circuit.
Dimensions: 45mm x 35mm x 7mm

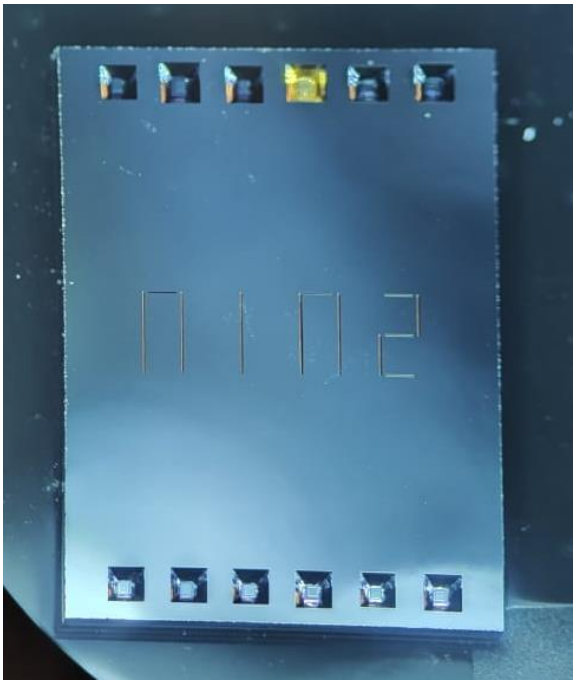

Figure 5.20. Non-symmetric quad-mass tuning fork gyroscope.
Dimensions: 8mm x 6.5mm x 0.9mm

The sensitivity of the FM gyroscope is set by the amplitude ratios and the angular gain of the structure. To analyze the effectiveness of the higher amplitude ratio of the FM gyroscope, performance tests were conducted for the ratios of 75, 500, and 2500. During these tests, Allan-Variance Analysis, temperature characterization of bias and scale factor are done.

For the 3 different amplitude ratios having constant first mode displacement, temperature characterization tests were conducted.

During the test, scale factor and bias values of the FM gyroscope is measured by using a rate table having temperature chamber as shown in Figure 5.21. The temperature inside this chamber is increased from 15°C to 55°C, and the tests were conducted in different temperature settings.

Figure 5.21. Temperature characterization setup for different amplitude ratios of the FM gyroscope

The increase in the amplitude ratio, did not worsen the scale factor change over temperature as shown in Figure 5.22.

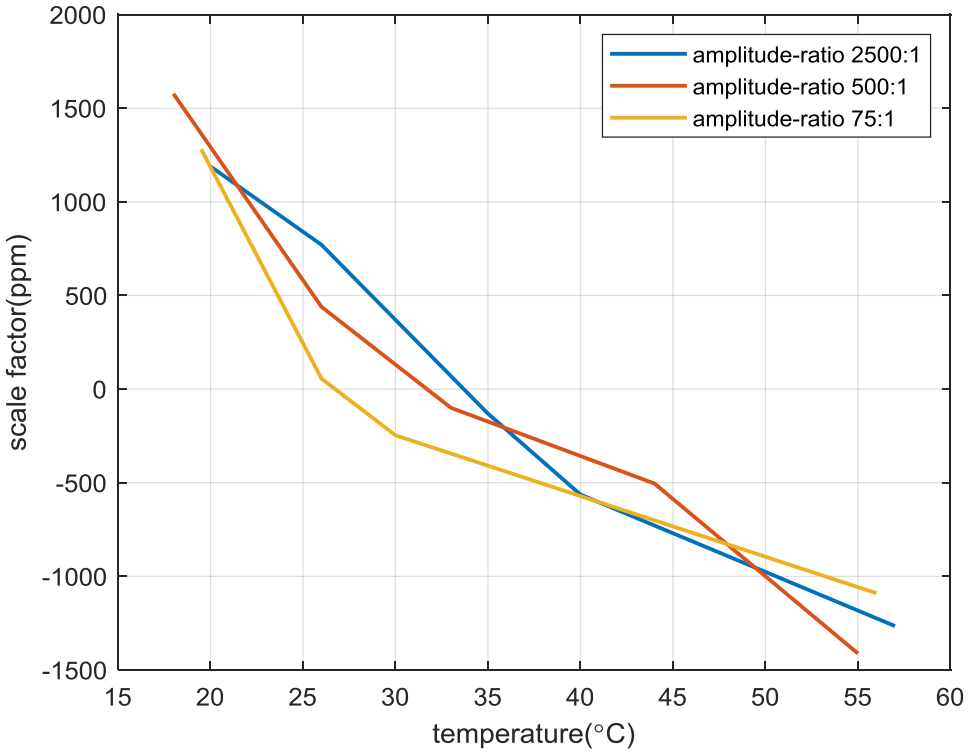

Figure 5.22. FM gyroscope scale factor test for different temperature values. The scale factor change in temperature is similar for 3 different amplitude ratios.

While conducting scale factor test, bias values of the sensors were also collected to compare the bias change over temperature. The increased amplitude ratio improved the bias change over temperature performance of the FM gyroscope from 35°/hr to 10°/hr over 15°C to 55°C as shown in Figure 5.23

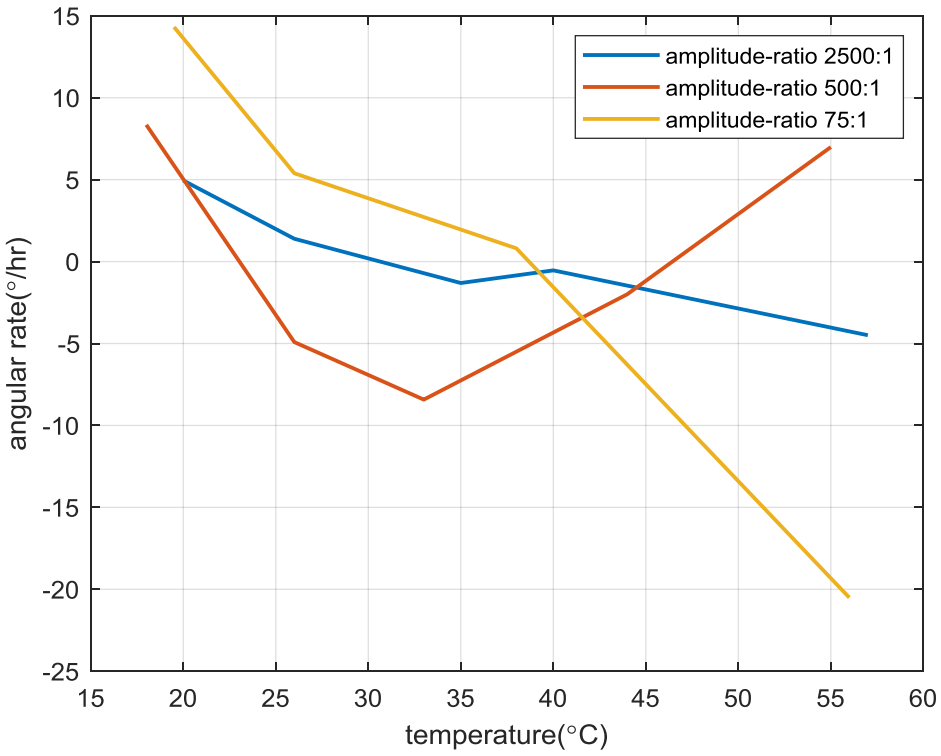

Figure 5.23. FM gyroscope bias change over temperature test result. Increased amplitude ratio improved the bias change from 35°/hr to 10°/hr over 15°C to 55°C.

To compare the effectiveness of the scale factor and bias change over temperature of the FM gyroscope over AM gyroscope, the gyroscope system is operated as AM during the temperature test. The AM operated gyroscope showed the scale factor change over temperature as about 8500ppm over 15°C to 55°C. When we compare the result with the FM gyroscope with a 2500 amplitude ratio, the FM gyroscope is three times better than the AM gyroscope, as shown in Figure 5.24.

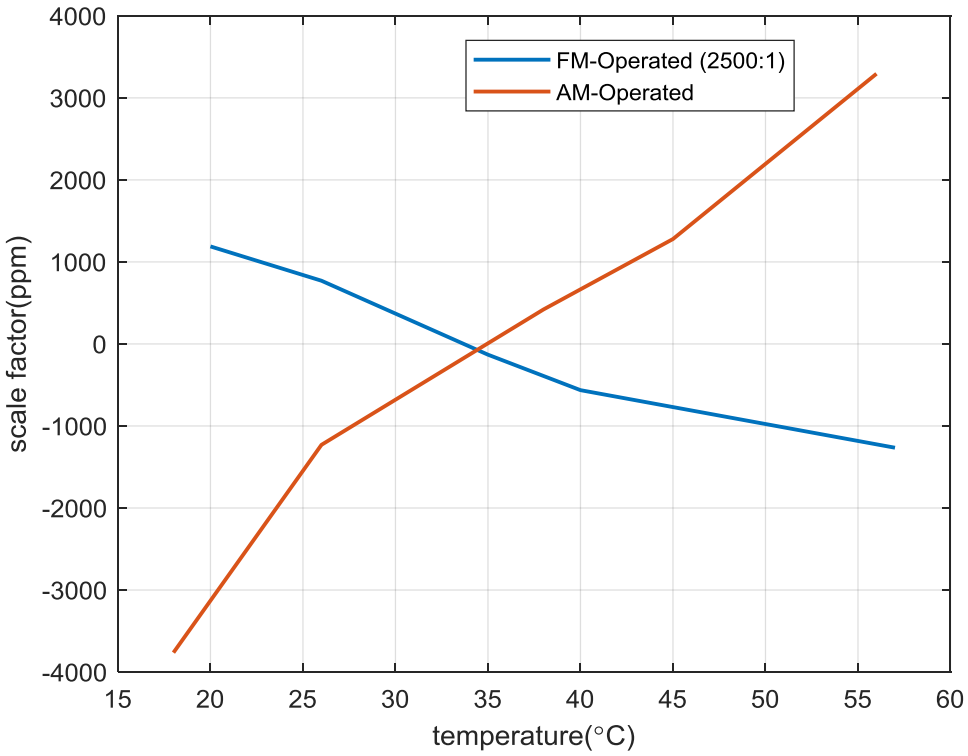

Figure 5.24. FM and AM gyroscope scale factor test for different temperature values. The scale factor change in temperature is 3 times higher for the AM gyroscope compared to the FM gyroscope.

After the scale factor test, the bias change over temperature test were conducted. Then, the bias change over temperature test results for the AM and FM cases are compared. The AM-operated gyroscope showed four times the change in bias over temperature that is obtained from an FM-operated gyroscope, as shown in Figure 5.25

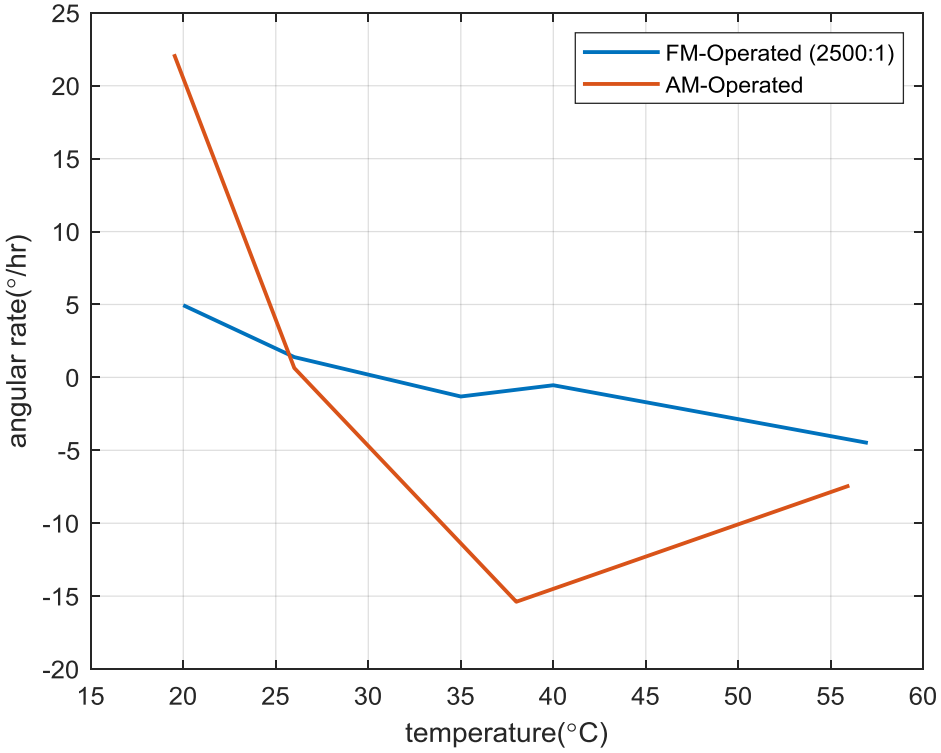

Figure 5.25. FM and AM gyroscope bias test for different temperature values. The bias change in temperature is 4 times higher for the AM gyroscope compared to the FM gyroscope.

The most important performance metrics for a gyroscope are angular random walk and bias instability. These are obtained by applying the Allan Variance Analysis for the collected rate data from the stationary FM operated MEMS gyroscope. During the test, rate data collected for 3 different amplitude ratios of 75, 50, and 2500. The test results for 3 different amplitude ratio FM MEMS gyroscope operations were analyzed as shown in Figure 5.26 to Figure 5.28 respectively. These results showed that, the increase in the amplitude ratio improves the angular random walk and bias instability performances of the FM MEMS gyroscope as inFigure 5.29.

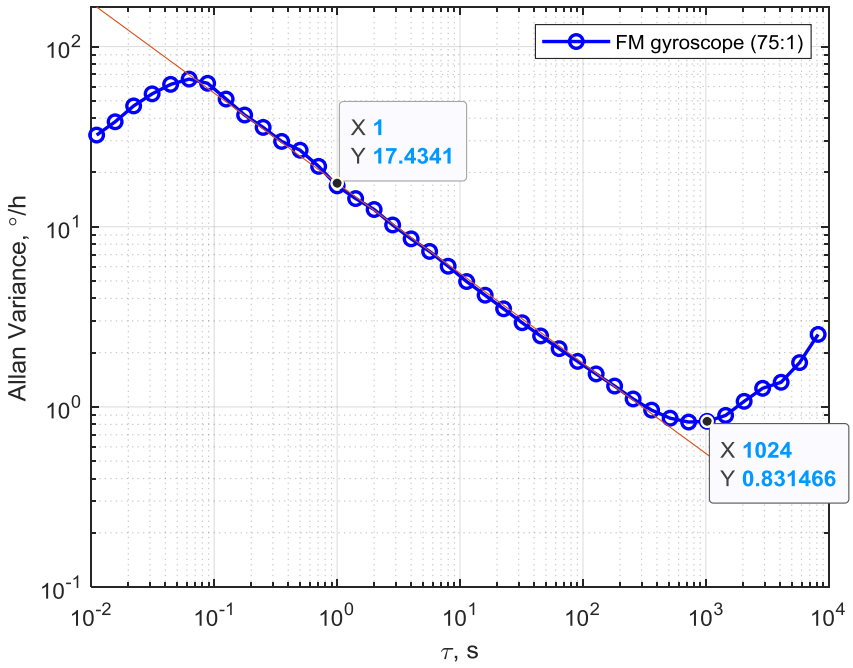

Figure 5.26. Allan Variance Analysis result for FM gyroscope operated with 75:1 amplitude ratio. ARW: 17.4°/hr/√Hz, BI: 0.83°/hr.

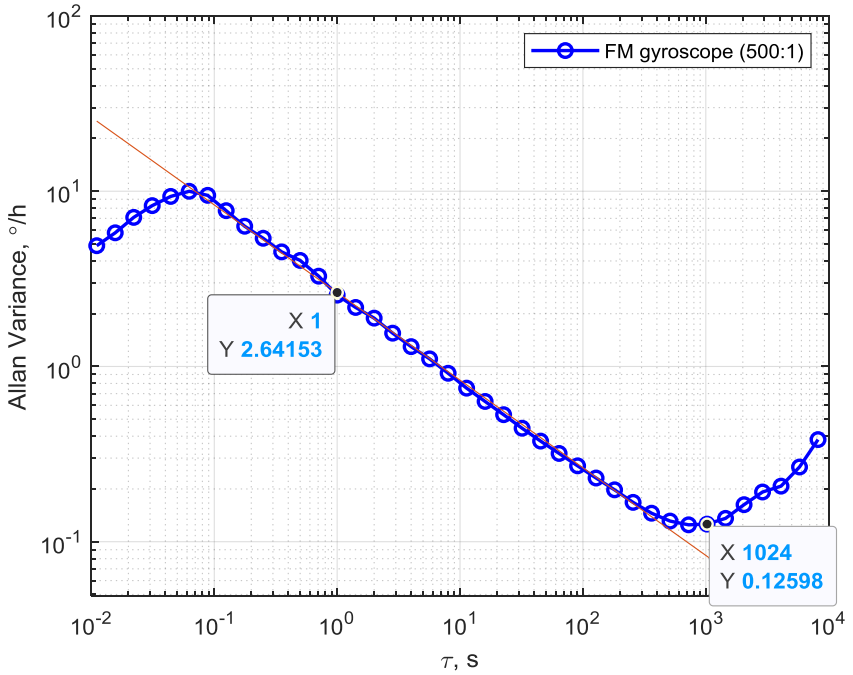

Figure 5.27. Allan Variance Analysis result for FM gyroscope operated with 500:1 amplitude ratio. ARW: 2.6°/hr/√Hz, BI: 0.13°/hr.

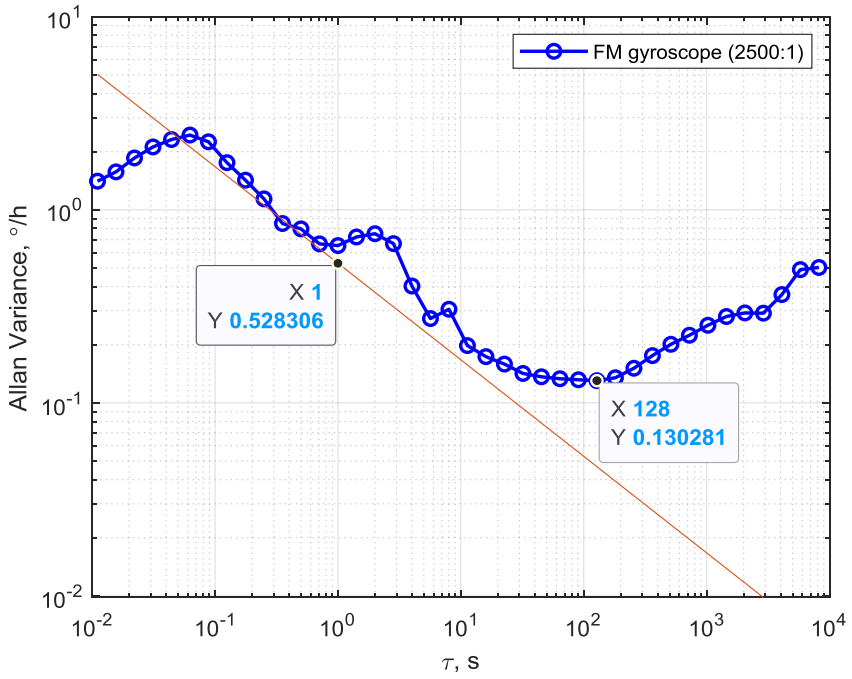

Figure 5.28. Allan Variance Analysis result for FM gyroscope operated with 500:1 amplitude ratio. ARW: 0.52°/hr/√Hz, BI: 0.13°/hr.

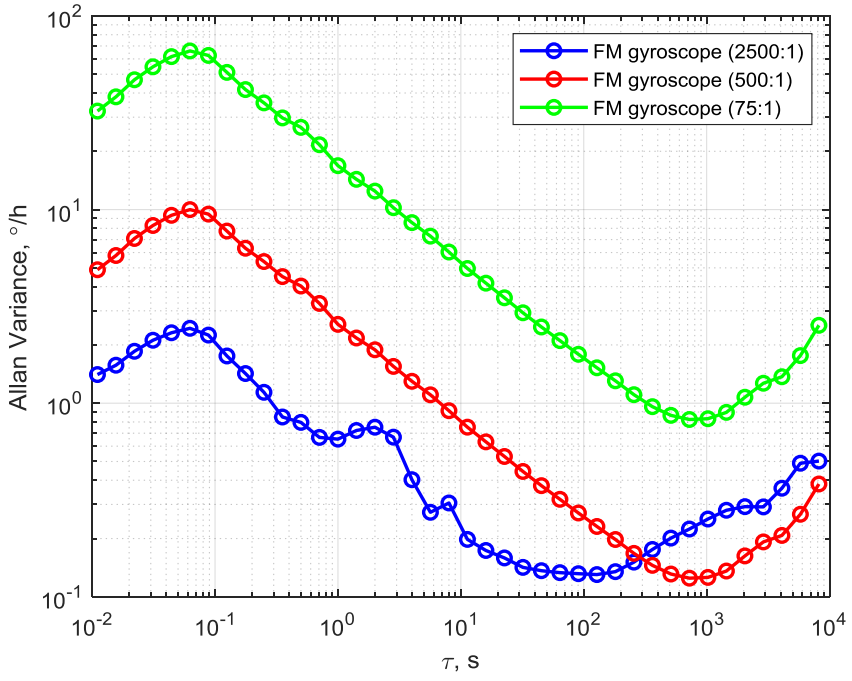

Figure 5.29. Allan Variance Analysis result for FM gyroscope operated with different amplitude ratios.

After getting the performance test results of the digitally controlled FM gyroscope matches with the theoretical results, Digital controller is configured as an AM gyroscope to compare the FM and AM operations in the digitally controlled operation.

In the FM operation the frequency split is adjusted as 20Hz to increase the performance of the gyroscope. However, in AM operation, the frequency split is arranged as 700Hz to operate the second mode of the gyroscope without stability problems. Thus, we obtained the performance results of this AM gyroscope as follow.

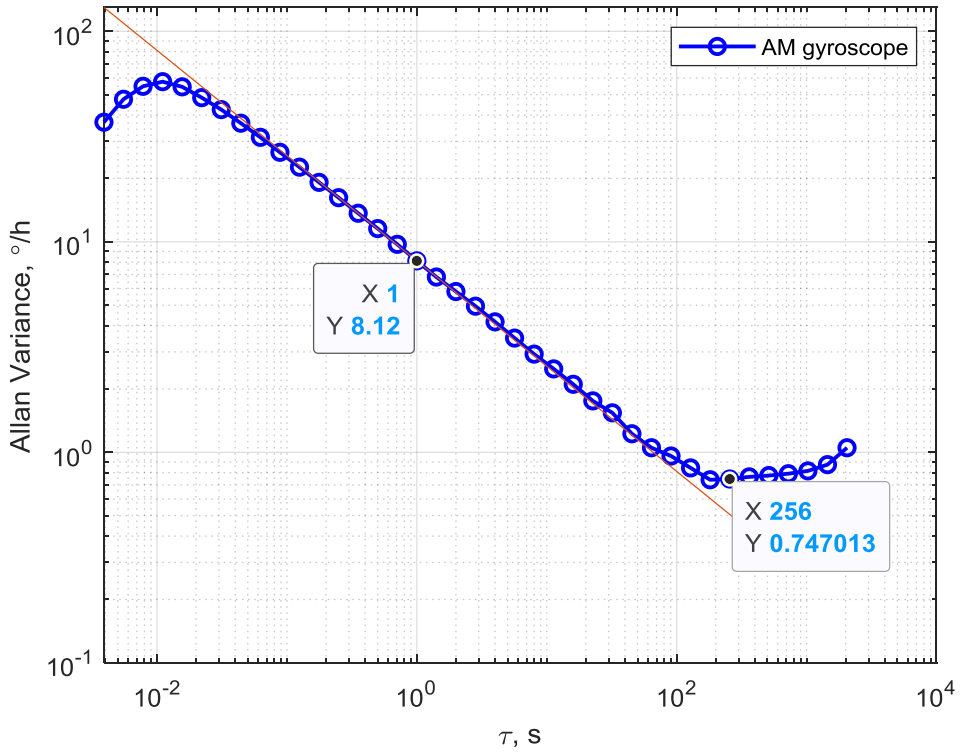

Figure 5.30. Allan-Variance Analysis of the digitally controlled AM gyroscope. ARW: 8.12°/hr/√Hz, BI: 0.74°/hr.

As it can be seen at Figure 5.30, the noise performance of the FM gyroscope is 16 times better than the AM gyroscope. The reason for this performance increase is the very low frequency split operation provided by FM operation and the increased amplitude mismatch to improve the frequency reading performance. The performance comparisons of the FM and AM operations can be seen at Figure 5.31.

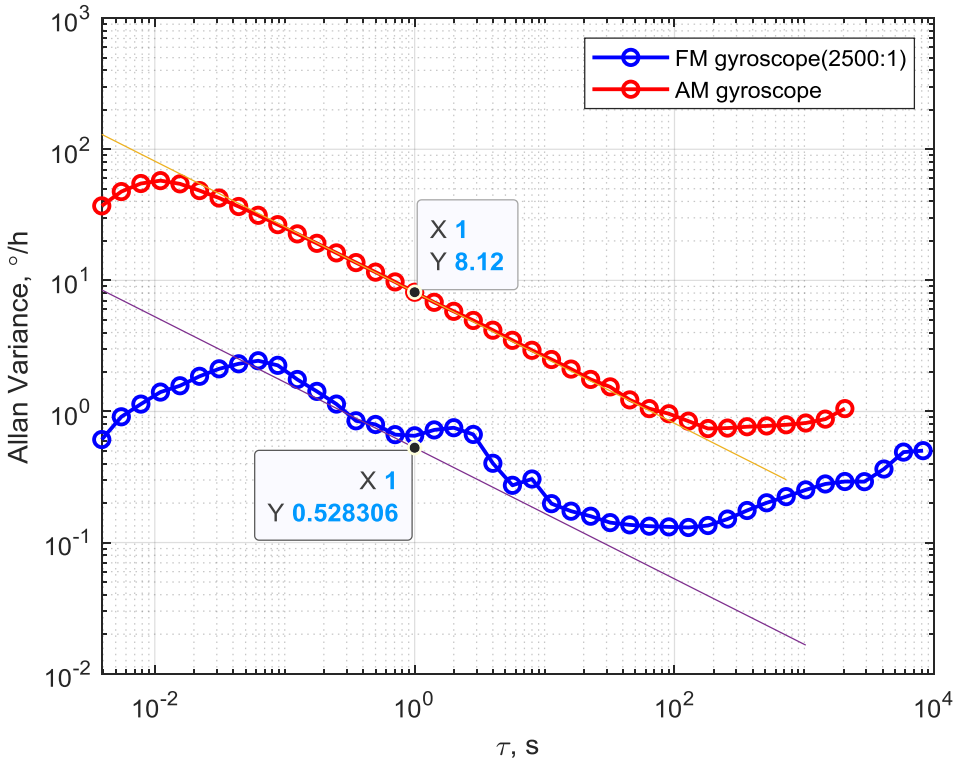

Figure 5.31. The comparison of the digitally operated FM and AM gyroscopes. ARW of FM: 0.52°/hr/√Hz, ARW of AM: 8.12°/hr/√Hz.

The performance of the digitally implemented FM gyroscope can also be compared with the FM gyroscope studies conducted with different researchers. The performance metrics can be Angular Random Walk (ARW), Bias Instability (BI), Mode split, read-out feature, etc. The Table 5.1 shows this comparison table.

Table 5.2 Summary and comparison table of the FM gyroscope performance.

	This work	Eminoglu[17]	Kline [16]	Wang[19]	Leoncini[32]
Angular Random Walk (ARW) (°/hr/√Hz)	0.5	3.6	17.6	18.9	112
Bias Instability (°/hr)	0.2	1.2	1.7	2.1	5.4
Mode-split (Hz)	20	10	26	9	104
Power Consumption (ASIC + FPGA)	300mW	>1W	>1W	>1W	>1W
Read-out Features	Digital oscillator sustaining loop and frequency processing with custom microcontroller board design	Analog ASIC for oscillator sustaining loop. Frequency and data processing with FPGA development board	Analog oscillator sustaining loop, Frequency and data processing with FPGA development board	Digital oscillator sustaining loop and frequency processing with custom FPGA board design	Analog ASIC for oscillator sustaining loop with a frequency to digital converter inside the ASIC.

Thus, The FM gyroscope implemented with digital oscillator sustaining loop and frequency processing with custom microcontroller board in this study has the lowest Angular Random Walk (ARW) and Bias Instability (BI) performance compared with other studies conducted on FM gyroscopes.

CHAPTER 6

CONCLUSIONS

The main goal of this study is to improve the angular random walk (ARW) and bias instability (BI) of a capacitive FM MEMS gyroscope by utilizing digital control loops implemented with a digital microcontroller. The most important parameter in an FM gyroscope is the frequency resolution. The frequency noise is analyzed and controlled with a sophisticated PLL design. The angular random walk and bias instability performance of the FM gyroscope is greatly improved by using a high amplitude mismatch ratio for the first and second modes, as well as utilizing Lissajous FM method. The following is a list of the research's accomplishments and outcomes:

1. An asymmetric tuning fork gyroscope has been analyzed at the system level for the first mode, the second mode, and the quadrature cancellation system. The transfer functions of the subsystems have been derived. Also, the mode-matching methods are explained, along with their pros and cons.

2. Next, the FM gyroscope is modeled in detail. The gyroscope system is modeled as two oscillators that are coupled to each other. This analysis shows that the forces that act together can change the effective damping and spring constant for both operational modes. Damping changes if the force is in sync with the speed. Similarly, the stiffness changes if the force is in sync with displacement. A standard FM gyroscope uses this second method resulting in the fact that the effective resonant frequency of both the first and second mode changes with the angular rate. The change in the resonant frequency by angular rate is typically much small compared to the mechanical resonant frequency of the sensor, which corresponds to a very high zero angular rate offset. In order to get rid of this offset, the Lissajous

FM gyroscope method is studied and the mathematical formulas are figured out to set up the system.

3. The resolution and stability of the oscillator frequency are the two important parameters that directly affects the angle random walk and bias instability performance of the FM gyroscope. The theory and operating principles of the oscillator is explained in detail. After that, the theory of the oscillator phase noise for both linear and non-linear models is derived. Next, a closed-loop oscillator phase noise analysis is done for both analog and digital controller-based systems including noise contributions of resonator, amplifiers, and data converters.

4. A digitally controlled and configurable (FM or AM) gyroscope system is designed, manufactured, and then the firmware is developed. The operation of a closed loop gyroscope with a digital microcontroller requires numerous calculations, including trigonometric conversions. As a rule of thumb, the speed of the digital controller loops must be greater than 10 times the resonant frequency of the selected MEMS gyroscope, which is around 7.5kHz. Selecting a microcontroller with a hardware accelerator and register level programming, a firmware is developed to accomplish the required calculations in only 12.5 μsec/cycle.

5. The developed FM gyroscope system is fully programmable allowing the user to select different operation modes with advanced digital controller implementations. This includes but not limited switching between FM to AM mode, frequency mismatch operation to matched-frequency operation, and/or sophisticated calibration and test methods that cannot be met by analog implementations (such as mode reversal). Furthermore, the completed system consists only of an ADC, a DAC, a microcontroller, and a power unit. In comparison to the analog implementation of the gyroscope readout circuit, the digital implementation is much simpler to manufacture due to the reduced number and type of components. The reduction of the number of analog components in the gyroscope controller circuits also helps minimizing the aging effects.

The PLL within the design of a digital controller is crucial for maintaining oscillation with low phase noise and reading the rate-dependent frequency from the PLL. A PLL design procedure is developed in order to track the frequency changes that occur at the frequency split between the two operational modes. In contrast to the standard PLL, the bandwidth of this PLL also determines the bandwidth of the gyroscope, which must be properly designed to fit the requirements of different applications. In this study, the PLL bandwidth is selected as 100Hz.

The rate noise performance of the developed FM gyroscope is estimated as 0.42°/hr/√Hz, which is quite close to the measured value of 0.52°/hr/√Hz.

The performance of the fabricated FM MEMS gyroscope is evaluated at the sensor level. The tested prototype achieved an extraordinary performance level by demonstrating an ARW of 0.52°/hr/√Hz and BI of 0.2°/hr. In order to compare the performance of the FM mode of the MEMS gyroscope to the AM mode, the digitally controlled FM gyroscope is reprogrammed to operate as an AM gyroscope. The AM gyroscope showed an ARW and BI performance of 8.12°/hr/√Hz and of 0.74°/hr, respectively. The results demonstrated that FM mode operation of this particular asymmetric MEMS gyroscope improves the ARW and BI performance by approximately 16 times and 3.5 times, respectively, compared to AM mode operation.

Finally**,** the results of the FM gyroscope developed in this study is compared with other FM gyroscopes reported in the literature**.** The novel FM techniques developed in this study applied to a commercial MEMS gyroscope developed by Mikrosistemler achieved the best Angular Random Walk (ARW) and Bias Instability (BI) performance among other FM gyroscope studies**.** These results motivate us to commercialize this new FM gyroscope in near future.

REFERENCES

[1] B. Eminoglu *et al*., "Comparison of long-term stability of AM versus FM gyroscopes," *2016 IEEE 29th International Conference on Micro Electro Mechanical Systems (MEMS)*, 2016, pp. 954-957,

[2] P. Greiff and B. Boxenhorn, "Silicon Monolithic Micromechanical Gyroscope," in *6th International Conference of Solid-State Sensors and Actuators*, San Francisco, CA, 1991.

[3] D. Xia, C. Yu and L. Kong, "The Development of Micromachined Gyroscope Structure and Circuitry Technology," Sensors, pp. 1394-1473, 2014.

[4] D. Lapadatu and B. Blixhavn, "SAR500 - A High-Precision High-Stability Butterfly Gyroscope with North Seeking Capability," in *Position Location and Navigation Symposium (PLANS 2010)*, IndianWells, CA, 2010.

[5] B. R. Johnson and E. Cabuz, "Development of a MEMS Gyroscope for Northfinding Applications," in *Position Location and Navigation Symposium (PLANS 2010)*, IndianWells, CA, 2010.

[6] B. Chaumet and B. Leverrier, "A New Silicon Tuning Fork Gyroscope for Aerospace Applications," in *Symposium Gyro Technology*, Karlsruhe, Germany, 2009.

[7] S. E. Alper, "MEMS Gyroscopes for Tactical-Grade Inertial Measurement Applications," in *Dissertation for the Degree of Doctor of Philosophy*, Middle East Technical University, 2005.

[8] E. Tatar, "Quadrature Error Compensation and Its Effects on the Performance of Fully Decoupled MEMS Gyroscope," in *M.S. Thesis*, Middle East Techical University, 2010.

[9] M. M. Torunbalci, S. E. Alper and T. Akin, "Wafer Level Hermetic Sealing of MEMS Devices with Vertical Feedthroughs using Anodic Bonding," *Sensors and Actuators A*, no. 224, pp. 169-176, 2015.

[10] M. M. Torunbalci, "Development of New, Simple, and Robust Wafer Level Hermetic Packaging Methods for MEMS Sensors," in *Ph.D. thesis*, METU, 2015.

[11] M. M. Torunbalci, H. D. Gavcar, F. Yesil, S. E. Alper and T. Akin, "An All-Silicon Process Platform for Wafer-Level Vacuum Packaged MEMS Devices," in *IEEE Sensors Journal*, vol. 21, no. 13, pp. 13958-13964, 1 July1, 2021,

[12] B. Eminoglu, "Control Electronics for MEMS Gyroscope and Its Implementation in a CMOS Technology," in *M.S. Thesis*, METU, 2011.

[13] H. D. Gavcar, "Compensation Methods for Quasi-Static Acceleration Sensitivity of MEMS Gyroscopes," in *M.S. Thesis*, Middle East Technical University, 2014.

[14] A. A. Seshia, R. T. Howe, and S. Montague, "An integrated microelectromechanical resonant output gyroscope," in *Proc. IEEE Int. Conf., 15th IEEE Int. Conf. Micro Electro Mech. Syst. (MEMS)*, Jan. 2002, pp. 722–726.

[15] H. Moussa and R. Bourquin, "Theory of direct frequency output vibrating gyroscopes," *IEEE Sensors J.*, vol. 6, no. 2, pp. 310–315, Apr. 2006.

[16] M. H. Kline *et al.*, "Quadrature FM gyroscope," in *Proc. IEEE 26th Int. Conf. Micro Electro Mech. Syst. (MEMS)*, Jan. 2013, pp. 604–608.

[17] B. Eminoglu, " High Performance FM Gyroscopes," in Ph.D. thesis, Berkeley, California, USA, 2017.

[18] G. Langfelder *et al.*, “Frequency modulated MEMS gyroscopes: Recent developments, challenges and outlook,” in *Proc. 20th Int. Conf. Solid-State Sens. Actuators Microsyst. Eurosensors (TRANSDUCERS EUROSENSORS)*, Jun. 2019, pp. 425–429.

[19] X. Wang *et al*., "A Digital Control Structure for Lissajous Frequency-Modulated Mode MEMS Gyroscope," in *IEEE Sensors Journal*, vol. 22, no. 20, pp. 19207-19219, 15 Oct.15, 2022.

[20] I. P. Prikhodko, J. A. Gregory, C. Merritt, J. A. Geen, J. Chang, J. Bergeron, W. Clark, and M. W. Judy, “In-run bias self-calibration for low-cost MEMS vibratory gyroscopes,” in *2014 IEEE/ION Position, Location and Navigation Symposium-PLANS 2014*, 2014, pp. 515–518.

[21] "IEEE Standard for Inertial Sensors Terminology," *IEEE Std 528-2001,* 2001.

[22] V. Uzunoglu, *Semiconductor Network Analysis and Design*, McGraw Hill, 1964, p.245.

[23] D. B. Leeson, “A simple model of feedback oscillator noises spectrum,” *Proc. IEEE*, vol. 54, pp. 329–330, Feb. 1966.

[24] B. Razavi, “A study of phase noise in CMOS oscillators,” *IEEE J. Solid-State Circuits*, vol. 31, pp. 331–343, Mar. 1996.

[25] A. Hadjimiri and T. H. Lee, “A General Theory of Phase Noise in Electrical Oscillators”, IEEE J. Solid-State Circuits, vol. 33, pp. 179-194, Febr. 1998.

[26] T. Remtema, "Active frequency tuning for micro resonators by localized thermal stressing effects," *Sensors and Actuators A: Physical*, pp. 326-332, 2001.

[27] B. Gallacher, J. Hedley and e. al., "Electrostatic correction of structural imperfections present in a microring gyroscope," *Journal of Microelectromechanical Systems*, vol. 14, no. 2, pp. 221-234, 2005.

[28] R. Antonello, "Automatic Mode Matching in MEMS Vibrating Gyroscopes Using Extremum-Seeking Control," *IEEE Transactions on Industrial Electronics*, pp. 3880-3891, 2009.

[29] C. D. Ezekwe and B. E. Boser, "A Mode-Matching Closed-Loop Vibratory Gyroscope Readout Interface With a 0.004 √Hz Noise Floor Over a 50 Hz Band," *IEEE Journal of Solid-State Circuits*, vol. 43, no. 12, pp. 3039-3048, 2008.

[30] F. Yesil, S. E. Alper and T. Akin, "An automatic mode matching system for a high Q-factor MEMS gyroscope using a decoupled perturbation signal," *2015 Transducers - 2015 18th International Conference on Solid-State Sensors, Actuators and Microsystems (TRANSDUCERS)*, 2015, pp. 1148-1151,

[31] Roland E. Best. Phase-Locked loops. McGraw-Hill, 1999.

[32] M. Leoncini, M. Bestetti, A. Bonfanti, S. Facchinetti, P. Minotti and G. Langfelder, "Fully Integrated, 406 μA, 5 ∘/hr, Full Digital Output Lissajous Frequency-Modulated Gyroscope," in *IEEE Transactions on Industrial Electronics*, vol. 66, no. 9, pp. 7386-7396, Sept. 2019.

CURRICULUM VITAE

Surname, Name: Yeşil, Ferhat

EDUCATION

Degree	Institution	Year of Graduation
MS	METU Electrical and Electronics Eng.	2015
BS	METU Electrical and Electronics Eng.	2012
High School	Eskişehir Fatih Science High School, Eskişehir	2007

WORK EXPERIENCE

Date	Institution	Enrollment
2015 - Present	Mikrosistemler LTD. Co.	Electronics Engineer
2012-2015	METU_MEMS Center	Electronics Engineer
2012 January – 2012 May	ASELSAN	Electronics Engineer

FOREIGN LANGUAGES

Advanced English

INTERNATIONAL CONFERENCE PUBLICATIONS

[1] F. Yesil, S. E. Alper and T. Akin, "An automatic mode matching system for a high Q-factor MEMS gyroscope using a decoupled perturbation signal," *2015 Transducers - 2015 18th International Conference on Solid-State Sensors, Actuators and Microsystems (TRANSDUCERS)*, 2015, pp. 1148-1151, doi: 10.1109/TRANSDUCERS.2015.7181131.

INTERNATIONAL JOURNAL PUBLICATIONS

[1] M. M. Torunbalci, H. D. Gavcar, F. Yesil, S. E. Alper and T. Akin, "An All-Silicon Process Platform for Wafer-Level Vacuum Packaged MEMS Devices," in IEEE Sensors Journal, vol. 21, no. 13, pp. 13958-13964, 1 July1, 2021, doi: 10.1109/JSEN.2021.3073928.